The cohesin ATPase cycle is mediated by specific conformational dynamics and interface plasticity of SMC1A and SMC3 ATPase domains

Marina Vitoria Gomes, Pauline Landwerlin, Marie-Laure Diebold-Durand, Tajith B Shaik, Alexandre Durand, Edouard Troesch, Chantal Weber, Karl Brillet, Marianne V Lemée, Christophe Decroos, et al.

Cell Reports

Article

The cohesin ATPase cycle is mediated by specific conformational dynamics and interface plasticity of SMC1A and SMC3 ATPase domains

Graphical abstract

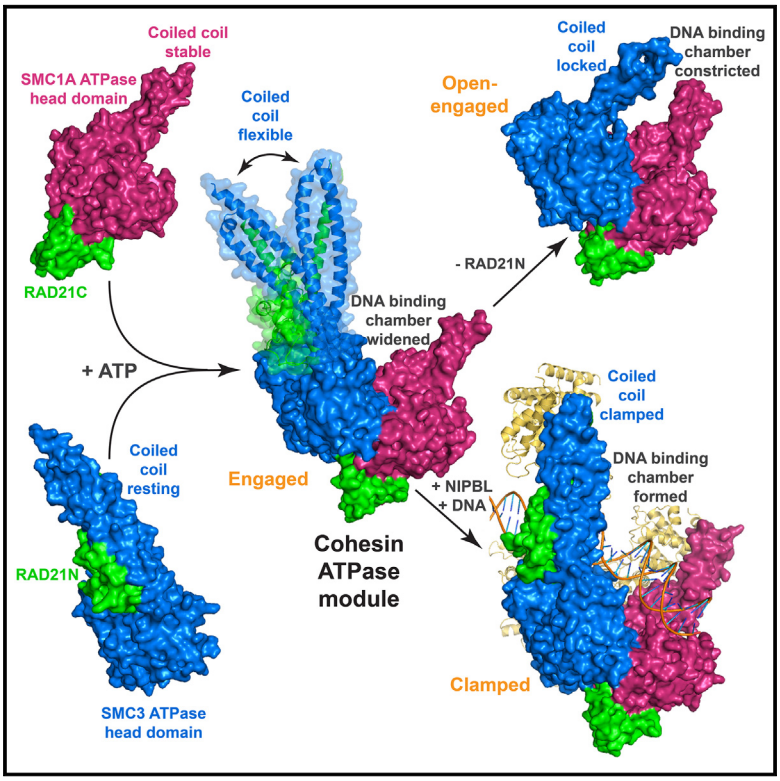

Highlights

- SMC1A and SMC3 ATPase domains show specific structural dynamics
- SMC3 ATPase domain proximal coiled coil has a specific intrinsic flexibility
- SMC3/RAD21 interface dissociation constricts SMC1A/SMC3 ATPase DNA-binding chamber
- SMC1A/SMC3 ATP interface plasticity allows dynamic moves but keeps the ATP gate shut

Authors

Marina Vitoria Gomes, Pauline Landwerlin, Marie-Laure Diebold-Durand, ..., Eric Ennifar, Christelle Golzio, Christophe Romier

Correspondence

romier@igbmc.fr

In brief

Vitoria Gomes et al. show that SMC1A and SMC3 ATPase domains have distinct, specific, but concerted conformational dynamics during the human cohesin ATPase cycle. Whereas the SMC1A proximal coiled coil is stable, that of the SMC3 has an intrinsic flexibility that modifies the size of the SMC1A/SMC3 ATPase module DNA-binding chamber.

Vitoria Gomes et al., 2024, Cell Reports *43*, 114656
September 24, 2024
https://doi.org/10.1016/j.celrep.2024.114656

CellPress

Cell Reports

CellPress
OPEN ACCESS

Article

The cohesin ATPase cycle is mediated by specific conformational dynamics and interface plasticity of SMC1A and SMC3 ATPase domains

Marina Vitoria Gomes,[1,2,3,4,8] Pauline Landwerlin,[1,2,3,4,8] Marie-Laure Diebold-Durand,[1,2,3,4,8] Tajith B. Shaik,[1,2,3,4] Alexandre Durand,[1,2,3,4] Edouard Troesch,[1,2,3,4] Chantal Weber,[1,2,3,5] Karl Brillet,[6] Marianne Victoria Lemée,[1,2,3,5] Christophe Decroos,[1,2,3,4] Ludivine Dulac,[1,2,3,4,5] Pierre Antony,[1,2,3,4] Erwan Watrin,[7] Eric Ennifar,[6] Christelle Golzio,[1,2,3,5] and Christophe Romier[1,2,3,4,9,*]

[1]Université de Strasbourg, IGBMC UMR 7104 – UMR-S 1258, 67400 Illkirch, France
[2]CNRS, UMR 7104, 67400 Illkirch, France
[3]INSERM, UMR-S 1258, 67400 Illkirch, France
[4]Institut de Génétique et de Biologie Moléculaire et Cellulaire, Department of Integrated Structural Biology, 67400 Illkirch, France
[5]Institut de Génétique et de Biologie Moléculaire et Cellulaire, Department of Translational Medicine and Neurogenetics, 67400 Illkirch, France
[6]Architecture et Réactivité de l'ARN, IBMC CNRS UPR 9002, Université de Strasbourg, 67084 Strasbourg Cedex, France
[7]CNRS, Université de Rennes, IGDR UMR 6290, 35000 Rennes, France
[8]These authors contributed equally
[9]Lead contact
*Correspondence: romier@igbmc.fr
https://doi.org/10.1016/j.celrep.2024.114656

SUMMARY

Cohesin is key to eukaryotic genome organization and acts throughout the cell cycle in an ATP-dependent manner. The mechanisms underlying cohesin ATPase activity are poorly understood. Here, we characterize distinct steps of the human cohesin ATPase cycle and show that the SMC1A and SMC3 ATPase domains undergo specific but concerted structural rearrangements along this cycle. Specifically, whereas the proximal coiled coil of the SMC1A ATPase domain remains conformationally stable, that of the SMC3 displays an intrinsic flexibility. The ATP-dependent formation of the heterodimeric SMC1A/SMC3 ATPase module (engaged state) favors this flexibility, which is counteracted by NIPBL and DNA binding (clamped state). Opening of the SMC3/RAD21 interface (open-engaged state) stiffens the SMC3 proximal coiled coil, thus constricting together with that of SMC1A the ATPase module DNA-binding chamber. The plasticity of the ATP-dependent interface between the SMC1A and SMC3 ATPase domains enables these structural rearrangements while keeping the ATP gate shut.

INTRODUCTION

Structural maintenance of chromosomes (SMC) complexes play key roles in genome organization in the three domains of life. While these complexes share a similar architecture and a common ATPase activity, they have evolved different functions supported by specific sets of core, auxiliary, and regulatory subunits.[1–3] How shared and evolutionary-divergent mechanisms of SMC complexes contribute to their specific functions remains poorly understood. Among the SMC complexes, eukaryotic cohesin participates in many functional processes throughout the cell cycle, notably sister chromatid cohesion, chromosome segregation, DNA repair, chromatin loop formation, and, in vertebrates, V(D)J recombination and formation of topologically associated domains. To perform these functions, cohesin acts in an ATP-dependent manner through different mechanisms, including dynamic loop extrusion and DNA tethering.[1,3]

The core cohesin complex is composed of two Smc subunits, SMC1A and SMC3, and of the RAD21^{Scc1} kleisin subunit (human names used throughout; *Saccharomyces cerevisiae* names given in superscripts when diverging significantly from human names). The SMC1A and SMC3 subunits harbor at each of their extremities a hinge domain and an ABC-transporter-like ATPase head domain (HD), both separated by a long intramolecular antiparallel coiled coil.[3–5] Formation of the cohesin core complex involves SMC1A and SMC3 heterodimerization through their hinge domains and the asymmetric bridging by RAD21^{Scc1} of the SMC1A- and SMC3-HDs to form the tripartite ring characteristic of SMC complexes (Figure 1A).[6–10]

In the presence of ATP, the cohesin SMC1A- and SMC3-HDs also heterodimerize upon binding two ATP molecules. ATP binding is driven in a composite manner by small ATP-binding motifs (Walker A/P-loop, Walker B, D-loop, Q-loop, R-loop, signature motif) contributed by both HDs at both ATP-binding sites.[5,6,8] ATP-dependent HDs heterodimerization, known as engagement, results in the formation of the cohesin ATPase module (engaged state) that dissociates upon subsequent ATP hydrolysis.[10–13] ATP binding and hydrolysis are key to most cohesin

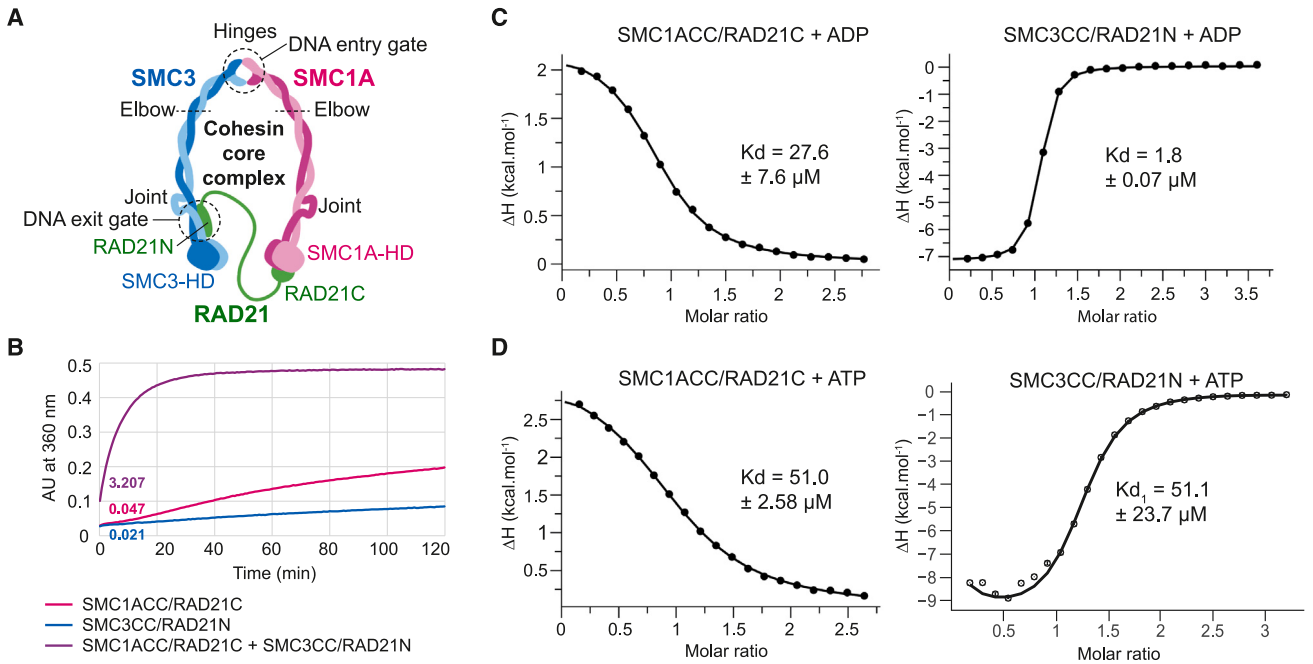

Figure 1. ATP hydrolysis and nucleotide-binding properties of human SMC1A and SMC3 ATPase head domains (HDs)

(A) Schematic representation of the human cohesin core complex. Specific elements discussed in the text are labeled.

(B) ATPase activity of the isolated and mixed SMC1ACC/RAD21C and SMC3CC/RAD21N complexes. The ATPase activity is given in Pi molecules released per dimer and per minute. All experiments were done in technical or biological triplicate.

(C) Measurements of the K_D of ADP for the SMC1ACC/RAD21C and SMC3CC/RAD21N complexes.

(D) Same as in (C) for ATP.

All experiments for (C) and (D) were done in technical or biological duplicate.

mechanisms and functions, and many cohesin auxiliary and regulatory subunits interact directly or in the vicinity of the non-engaged or ATP-engaged SMC1A- and SMC3-HDs.[10–12,14]

Among cohesin regulatory subunits, NIPBL^{Scc2} was shown to stimulate ATP hydrolysis by the cohesin ATPase module, a stimulation required for cohesin loop extrusion.[15–18] The structures of yeast and human cohesin ATPase modules in complex with NIPBL^{Scc2} and DNA have revealed how the protein components encircle and clamp the non-topologically bound DNA (clamped state).[10–12] By which mechanisms NIPBL^{Scc2} stimulates the cohesin ATPase activity is, however, still unclear. NIPBL^{Scc2} also plays an initial role in cohesin DNA tethering by causing the ATP-dependent topological entrapment of DNA within the cohesin ring through the hinge/hinge interface (DNA entry gate; Figure 1A).[12,17,19–25]

The mechanisms subsequently leading to cohesin genomic stabilization and then to genomic removal also require ATP binding and hydrolysis but are independent of NIPBL^{Scc2} and rely on the PDS5 regulatory subunit. Specifically, cohesin genomic stabilization requires association with PDS5, which is favored by the acetylation of the SMC3-HD lysines K105 and K106 and is stabilized by SORORIN.[24,26–35] Cohesin genomic removal also requires PDS5, but when bound to WAPL, DNA release occurring through opening of the SMC3/RAD21 interface (DNA exit gate; Figure 1A).[20,26,28,31,36–43] The different mechanisms participating in cohesin DNA tethering and release remain poorly characterized at the molecular level but are equally essential to cohesin functions and act in synergy with loop extrusion to regulate the length of chromatin loops and to shape the eukaryotic three-dimensional genome in an ATP-dependent manner.[43–49]

An essential characteristic of cohesin is its intrinsic flexibility, which is required for its transactions with DNA and for its biological functions. Cohesin can adopt open ring, rod, and kinked conformations depending on whether the SMC1A and SMC3 coiled coils are interacting by co-alignment and are bent at their elbow elements.[10–12,14,39,50–53] The mechanisms by which cohesin alternates between these conformations remain unclear. The cohesin ATPase cycle is expected to be key to these conformational changes. However, the specific structural rearrangements occurring within the cohesin SMC1A- and SMC3-HDs and ATPase module during the cohesin ATPase cycle and how these can be propagated at long distance are poorly characterized.

Therefore, while cohesin ATPase activity is at the heart of the mode of action and functions of this SMC complex, the mechanisms that underlie this activity require further analyses. Here, we have characterized distinct steps of the human cohesin ATPase cycle. We show that the SMC1A and SMC3 ATPase HDs undergo highly specific structural movements and conformational rearrangements upon ATP binding, ATP-dependent engagement, ATP hydrolysis, and opening of the SMC3/RAD21 interface. These movements and rearrangements are different in both HDs but concerted between them. We notably reveal the intrinsic flexibility of the SMC3-HD proximal coiled coil and the high plasticity of the ATP-dependent interface between the

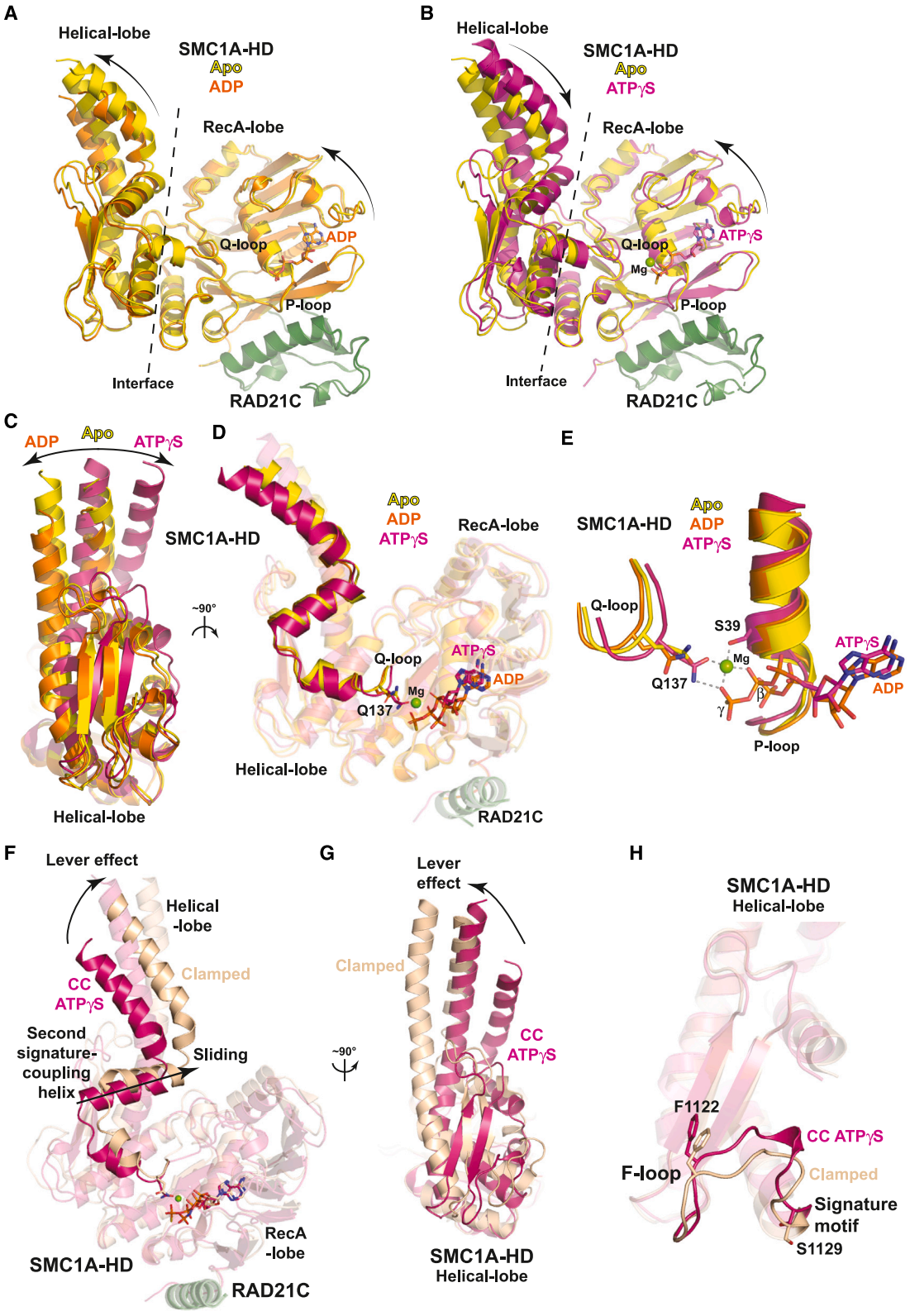

(legend on next page)

SMC1A- and SMC3-HDs that underlie the conformational dynamics of these HDs. Our results show the importance of the full N-terminal region of RAD21 in these mechanisms. Our results provide a most complete view of the cohesin ATPase cycle conformational dynamics that support cohesin mechanisms and functions.

RESULTS

Human SMC1A and SMC3 ATPase HDs have distinct nucleotide-binding properties and recapitulate the ATPase activity of the full core cohesin complex

Characterization of the cohesin complex in molecular terms is rendered difficult by the large flexibility of this complex. We used the isolated SMC1A- and SMC3-HDs to obtain the high-resolution data required to study in precise molecular terms the conformational dynamics of these HDs. Different constructs of the human SMC1A- and SMC3-HDs were made (see the STAR Methods) by varying the length of the proximal coiled coil (CC) emerging from their globular domains (GDs; Figures S1 and S2). RAD21N and RAD21C constructs were designed according to previous work (Figure S3).[6,8] Whereas single expression of these constructs led to insoluble proteins, their co-expression led to the soluble production of the various SMC1A-HD/RAD21C and SMC3-HD/RAD21N complexes. The SMC1ACC/RAD21C and SMC3CC/RAD21N complexes, which do not include the joint elements of the HDs, were chosen as primary targets for our investigations unless stated otherwise.

The SMC1ACC/RAD21C and SMC3CC/RAD21N complexes had a very low ATPase activity when analyzed independently, but a significant increase in activity was observed upon their mixing (Figure 1B). The ATPase activity of 3.2 Pi molecules released per dimer and per minute that we measured for the mixed HDs is within the range (~2.4–4.0) measured for the full-length human core cohesin complex obtained either using the baculovirus expression system or endogenously purified from HeLa cells.[15,16,24] This shows that the isolated HDs used in our study can recapitulate the ATPase activity of the full core cohesin complex.

Isothermal titration calorimetry (ITC) measurement of the dissociation constant (K_D) of nucleotides for the individual SMC1ACC/RAD21C and SMC3CC/RAD21N complexes was performed with both wild-type (WT) and low ATPase activity EQ mutants (SMC1A-E1157Q and SMC3-E1144Q) as well as with ATP and the low hydrolyzable ATPγS analog. The measured K_D values were all in the micromolar range, only showing some variations depending on the nucleotide analyzed (Figures 1C, 1D, S4A, and S4B; Table S1). Binding of nucleotides to these two complexes showed, however, different entropic and enthalpic contributions. Specifically, nucleotide binding was entropy driven for SMC1ACC/RAD21C and enthalpy driven for SMC3CC/RAD21N (Figures S4C and S4D).

X-ray crystallography was then used to investigate the molecular properties of the independent SMC1A-HD/RAD21C and SMC3-HD/RAD21N complexes and their binding to nucleotides. Crystallization assays were performed without nucleotides or in the presence of either ADP or ATPγS. All complexes crystallized in apo form and in complex with these nucleotides. The crystals obtained diffracted between 1.4 and 3.1 Å resolution (Tables S2–S4). Structure determinations were carried out by molecular replacement.

The SMC1A-HD/RAD21C complex shows Q-loop-based rotational movements but remains in a specific relaxed conformation upon nucleotide binding

The SMC1A-HD/RAD21C structures showed that the SMC1A-HD P-loop adopts, in the absence of nucleotides, a closed conformation that is stabilized by a network of water molecules interacting with neighboring residues (Figures S5A and S5B). Nucleotide binding therefore requires the release of this water network, which could agree with the observed entropy-driven binding of ADP and ATP to the SMC1ACC/RAD21C complex through a disorder increase. In addition, in all structures, R-loop R57 stably interacts with N40 and D43 and, in the presence of ATPγS, with the α-phosphate group of this nucleotide (Figures S5C and S5D). This contrasts with fungi where the Smc1 R-loop is not defined in density unless in the clamped state.[8,11,13] Mutation of R57 into alanine (R57A) or the use of the Cornelia de Lange syndrome (CdLS)-characterized 58–62 deletion mutant (Δ58-62)[54] caused a complete loss of ATP hydrolysis by the isolated SMC1A-HD (Figure S5E). However, this loss was only ~10% when SMC3CC/RAD21N was added to the reaction, indicating that human SMC1A R57 plays an early role in organizing the SMC1A-HD nucleotide-binding site prior to engagement.

Comparative analysis of the SMC1ACC/RAD21C structures revealed specific conformational changes occurring upon ADP and ATPγS binding that cause the movement of the RecA lobe and helical lobe of this HD with respect to each other. Notably, ADP binding causes a slight rotational movement of both lobes away from each other, whereas ATPγS binding brings both lobes closer to each other (Figures 2A and 2B). These rotational movements occur in the same plane that goes through the Q-loop (Figures 2C and 2D; Video S1). Specifically, upon ATPγS binding, Q137 moves toward the nucleotide binding site and binds to the Mg ion (1.9 Å), and hydrogen bonds to the

Figure 2. Specific conformational dynamics of SMC1A-HD

(A) Conformational movements within the SMC1A-HD upon ADP binding.
(B) Same as in (A) upon ATPγS and Mg binding.
(C) Opposite rotational movements of SMC1A-HD helical lobe upon ADP and ATPγS binding.
(D) The movements observed in (D) are in the same plane that goes through Q137.
(E) Close-up of (D) on the Q-loop.
(F) Movements of the helical lobe with respect to the RecA lobe of SMC1A-HD upon formation of the clamped complex.
(G) Same as in (F) in a 90° view focusing on SMC1A-HD helical lobe.
(H) Conformational and positional changes occurring in SMC1A-HD F-loop and signature motif upon formation of the clamped complex.

γ-thiophosphate group (2.6 Å) (Figure 2E). These movements do not induce significant structural changes to the RecA lobe/helical lobe interface and within the helical lobe itself, including to the F-loop and signature motif, but position differently the SMC1A proximal coiled coil depending on the nucleotide bound (Figure 2C).

In contrast, comparison of our SMC1ACC/RAD21C structures with that of the SMC1A-HD in the clamped state[10] revealed a large movement of the SMC1A-HD helical lobe with respect to the RecA lobe upon formation of the clamped state (Figure 2F). This movement, which has been called the lever effect in the bacterial/archaeal case,[55] is due to a sliding of the helical lobe along the RecA lobe. The amplitude of this movement is large, as demonstrated by the displacement by ∼7–8 Å of the second signature-coupling helix of SMC1A that precedes the N-terminal coil of this HD (Figure 2F). The lever effect also repositions the SMC1A CC in a central position (Figure 2G), as observed in our apo structure, but keeps Q137 at a close distance to the ATP molecule.[10]

Whereas the overall structure of the SMC1A helical lobe is not significantly modified by the lever effect in the clamped state, the F-loop and signature motif of this lobe undergo significant conformational and positional changes when compared to the isolated SMC1A-HD (Figure 2H). This also requires a significant reorganization of the RecA lobe/helical lobe interface. Importantly, the sliding movement upon leverage is almost perpendicular to the aforementioned planar rotational movement observed upon ADP and ATPγS binding to the isolated SMC1A-HD, showing that these conformational changes are not related (Figures 2D and 2F; Video S1). This demonstrates that when isolated, the SMC1A-HD adopts a stable relaxed conformation, regardless of its nucleotide-binding state, which is different from that of the clamped state.

Of note, our crystallographic structures of the SMC1ACCsh/RAD21C complex, where the SMC1A-HD proximal coiled coil is shorter than in the SMC1ACC/RAD21C complex, show a higher structural resemblance to that of the clamped SMC1A-HD. These structures notably display, as in the clamped conformation, a lever effect, a central repositioning of the SMC1A CC, a specific RecA lobe/helical lobe interface, and a conformational rearrangement of the F-loop and signature motif compared to the SMC1ACC/RAD21C structures (Figures S6A–S6C). These features appear, however, artificially induced by the crystal packing of the SMC1ACCsh/RAD21C complex that involves the SMC1A-HD proximal coiled coil but not the ATP-binding interface (Figures S6D and S6E). This shows that the reorganization of the SMC1A-HD F-loop requires only the rearrangement of the RecA lobe/helical lobe interface.

The SMC3-HD/RAD21N complex adopts a relaxed conformation with a specific resting state of the SMC3-HD proximal CC due to the interaction of RAD21N with the SMC3-HD GD

In the case of the isolated SMC3CC/RAD21N complex, our structures show a higher similarity whatever their nucleotide-binding state, with smaller adaptative movements observed upon binding of ADP and ATPγS and fewer water molecules displaced that could account for the observed enthalpy-driven binding mechanism (Figure 3A; Video S2). In addition, in all our structures, the SMC3 Q-loop is positioned far away (∼9 Å) from the nucleotide-binding site, with the Q141 side chain turned away from this binding site, even when ATPγS and magnesium are bound (Figure 3B; Video S2). This specific conformation is also different from that of the SMC3-HD in the clamped state, showing that this HD also adopts a relaxed conformation when isolated (Figure 3C).

Accordingly, to reach the clamped conformation, the SMC3-HD also requires a lever effect that slides its helical lobe along its RecA lobe, moving the SMC3 second signature-coupling helix by ∼4–5 Å (Figures 3C and 3D). The associated conformational changes affect the positioning and conformation of the Q-loop, repositioning Q141 toward the ATP-binding site (Figures 3C and 3D; Video S2). Other additional changes, specific to the SMC3-HD, are also observed that are reminiscent of those observed upon bacterial/archaeal Smc-HD homodimerization.[55] These include the conformational rearrangement of the wedge element, which turns away from the SMC3 CC toward the R-loop and accompanies the repositioning and conformational change of this loop and the repositioning but not the conformational rearrangement of the loop harboring the SMC3 signature motif (Figure 3D).

The most striking difference observed, however, is the ∼45° kink in our structures of the CC emerging from the SMC3 GD compared to the straight conformation displayed by this CC in the clamped complex (Figures 4A–4C; Video S2). This kink is due to a simultaneous bending of both α-helices forming the human SMC3 CC that occurs right above the region where these helices emerge from the SMC3 GD and just below the region where they interact with RAD21N (Figures 4A and 4B). The intrinsic flexibility of the short helical stretches of the SMC3 CC that enables their bending is demonstrated by their slightly different conformations observed in our different structures, including between non-crystallographic symmetry mates in a single crystal form.

The SMC3 CC kink is observed in all our SMC3CC/RAD21N structures, regardless of the nucleotide-binding state, which could account for their higher structural similarity. Although the folding of RAD21N and its interaction with the SMC3 CC are not changed by the kink, the new path of the SMC3 CC positions differently the RAD21 50-residue small N-terminal helical domain (HelD), which precedes the long RAD21N α helix interacting with the SMC3 CC, in the groove at the interface between the RecA lobe and helical lobe of the SMC3 GD (Figure 4B). The interactions formed between the RAD21N HelD and the SMC3 GD stabilize this specific conformation of the SMC3-HD/RAD21N interface that we have called resting state (Figure 4D).

Notably, the first small α helix of the RAD21N HelD, composed of residues 13–23, packs against the SMC3 GD. Following this helix, RAD21N K25 and K26 side chains interact, respectively, with the SMC3 GD D120 and D92 side chains. In addition, the R54 guanidino group makes several interactions with the SMC3 GD, notably with the acidic patch formed by the side chains of S131, S133, and D1135 (Figure 4D). In the clamped state, the RAD21N HelD is positioned above the SMC3 GD, both domains only forming a single contact through the interaction established between the RAD21N R54 side chain and the

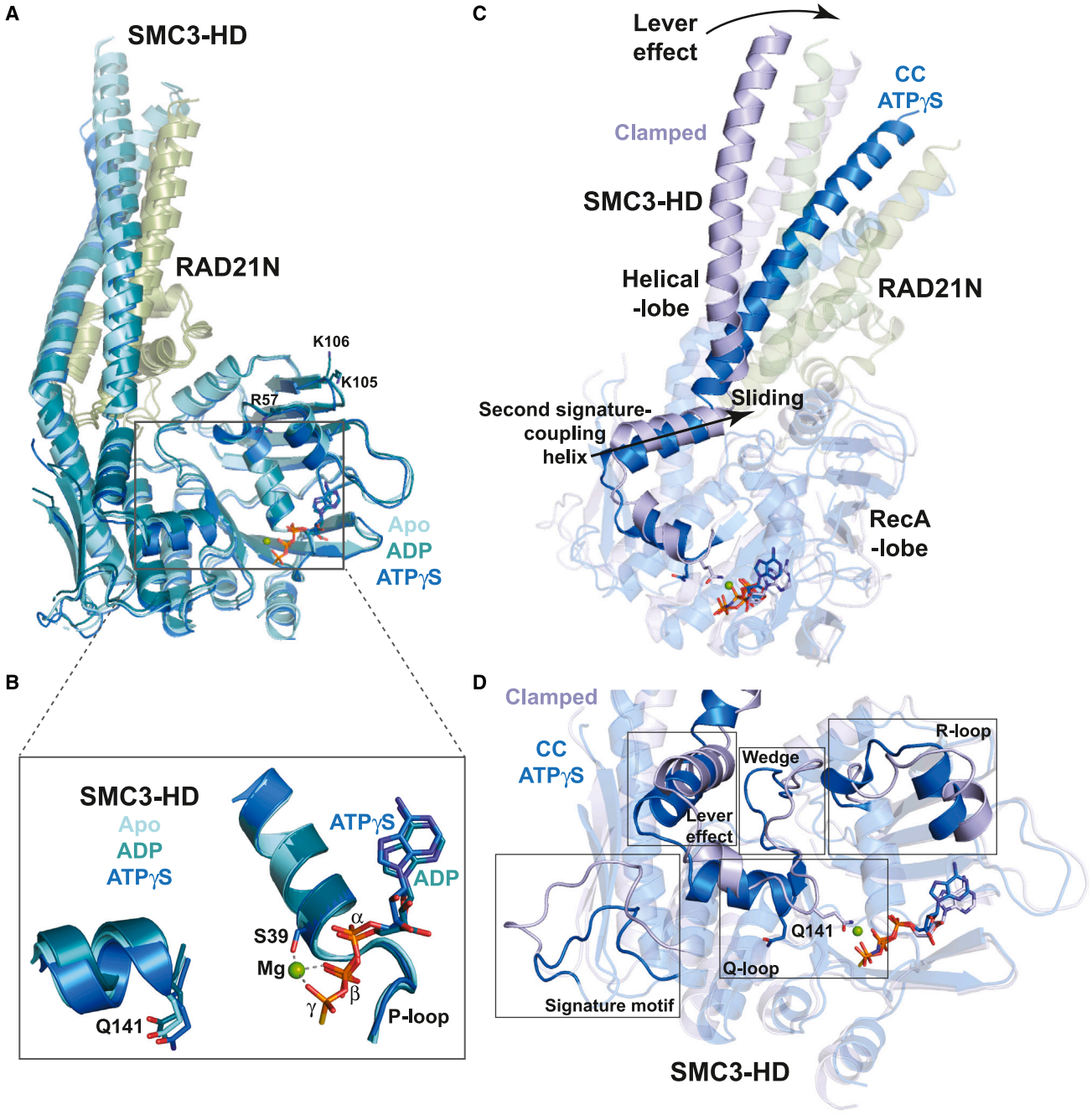

Figure 3. Specific conformational dynamics of SMC3-HD

(A) Superposition of the SMC3CC/RAD21N structures in various nucleotide-binding states (apo, ADP-bound, and ATPγS-bound).

(B) Close up on the ATP-binding site of the structures shown in (A).

(C) Conformational changes of SMC3-HD upon formation of the clamped complex.

(D) Multiple specific changes in SMC3-HD induced by the formation of the clamped complex.

SMC3 N123 main chain carbonyl (Figure 4E). In addition, the RAD21N HelD interacts with the bound DNA through electrostatic interactions and direct contacts, such as those that can be formed by RAD21N K25 and K26 with the DNA phosphate backbone.[10]

Importantly, the position of RAD21N in the resting state, notably its long α helix interacting with the SMC3 CC, is not compatible with the forward movement of the SMC3 second signature-coupling helix that occurs upon leverage (Figure 4F). Therefore, SMC3 is kept in its resting

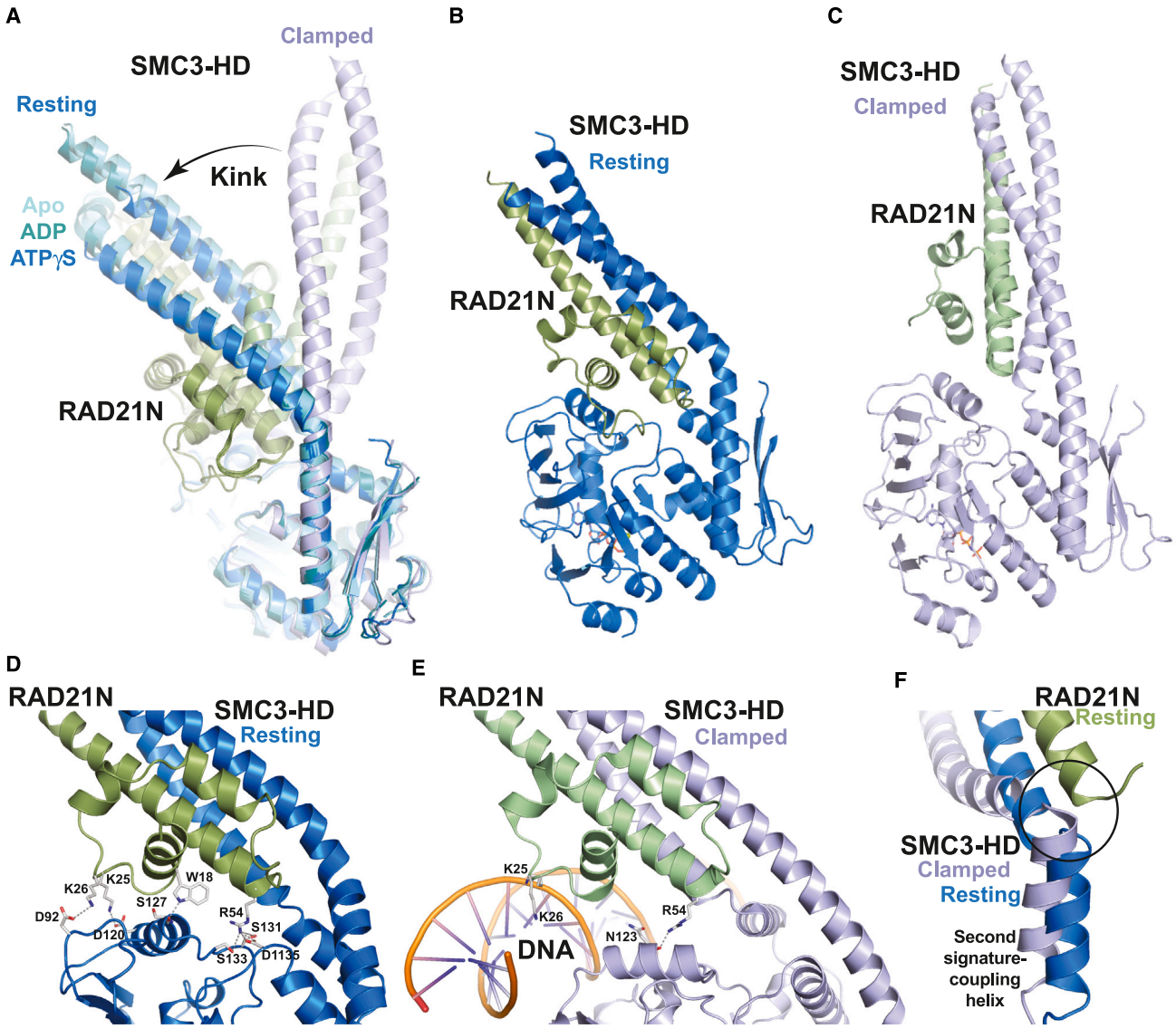

Figure 4. The SMC3-HD/RAD21N complex adopts a stable resting state

(A) Comparison of the structures of the isolated SMC3-HD/RAD21N complex with that in the clamped conformation.

(B) Structure of the SMC3-HD/RAD21N complex in its resting state showing the positioning of the RAD21N HelD domain at the interface between the RecA lobe and the helical lobe of the SMC3-HD.

(C) Same as in (B) for the SMC3-HD/RAD21N complex in its clamped conformation.

(D) Interactions made by the RAD21N HelD domain with the SMC3 GD in the resting state.

(E) Interactions made by the RAD21N HelD domain with the SMC3 GD and the DNA in the clamped complex.

(F) Steric clashes (circled) between the SMC3-HD second signature-coupling helix in the clamped conformation and the RAD21N long α helix paralleling the SMC3-HD CC in the resting state.

state through stabilization of the RAD21N HelD onto the SMC3 GD.

ATP-dependent engagement of the SMC1A- and SMC3-HDs induces large conformational changes that do not fully recapitulate those observed in the clamped state

To further characterize the cohesin ATPase cycle, we investigated the conformational dynamics of the SMC1A- and SMC3-HDs upon their ATP-dependent engagement. We first looked at conditions causing stable HDs interaction by using size exclusion chromatography, since weakly formed complexes cannot resist the dilution conditions of this technique. Analytical ultracentrifugation was used to confirm the results obtained. Initial analyses with the WT and EQ constructs revealed that only the SMC1ACC-EQ/RAD21C and the SMC3CC-EQ/RAD21N mutant complexes can stably associate when ATP is present (Figures 5A

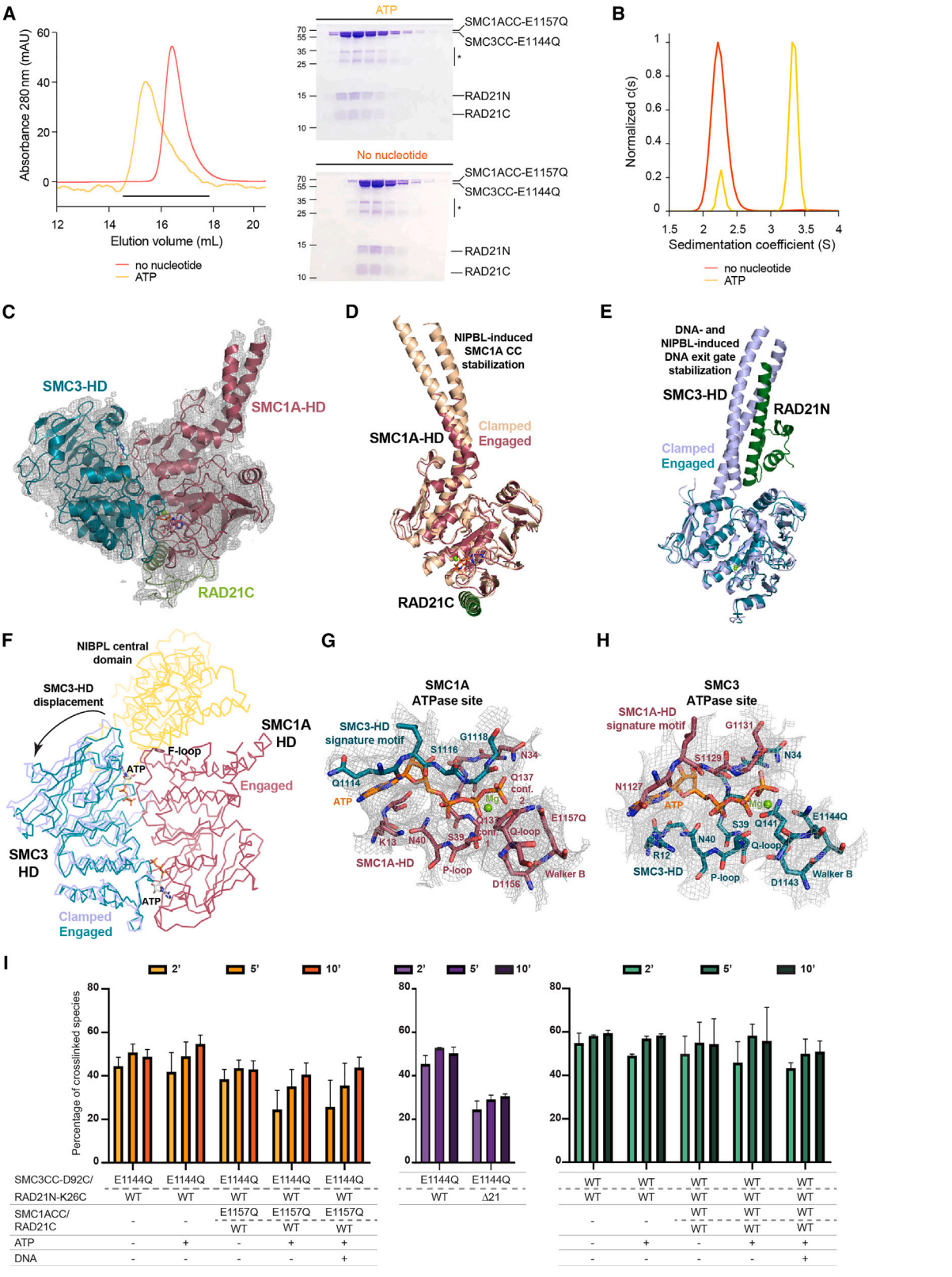

(legend on next page)

and 5B). Injection of the two EQ mutants on the ATP-loaded chromatographic column without preincubation with ATP was sufficient to form the complex, demonstrating its rapid assembly and stability. In contrast, combination of WT/WT, WT/EQ, and EQ/WT complexes failed to provide a stably engaged ATPase module in the presence of ATP (Figure S7A).

In addition, both size exclusion chromatography and analytical ultracentrifugation showed that while ATP causes engagement, ADP, ATPγS, and adenylyl-imidodiphosphate (AMP-PNP) cannot (Figure S7B), in agreement with previous observations on the yeast ATPase module.[23] Moreover, we did not observe a homodimerization of the independent SMC1ACC-EQ/RAD21C and SMC3CC-EQ/RAD21N mutants in the presence of ATP, demonstrating the specificity of the heterodimeric engagement (Figure S7C). Mutants in the signature motifs (SMC1A L1128V and SMC3 L1115V) and D-loops (SMC1A D1163E and SMC3 D1150E) have previously been shown, like the EQ mutants, to have low ATPase activity and to enable engagement.[26,56,57] However, no combination of these mutants yielded stable engagement in our experimental conditions (Figure S7D).

We used our stable engaged ATPase module for structural analyses. Crystallization attempts of the complex only yielded poorly diffracting crystals, and cryoelectron microscopy (cryo-EM) was used instead. Processing of the collected data yielded two cryo-EM maps at 3.6 and 4.4 Å resolution, both representing engaged complexes (Figure S8). Local resolution estimations (Figures S9A and S9B) showed that the GDs were better defined in both maps than the proximal coiled coils, suggesting a higher mobility of the latter, in agreement with previous cryo-EM works.[10–14] The best-resolved 3.6-Å map was used to solve the structure of the engaged human cohesin ATPase module. We established a first model of this module by fitting our high-resolution crystallographic structures into this map. This model was further refined by cycles of manual building and automatic real space refinement (Figures 5C and S9; Table S5).

The refined structure of the engaged human cohesin ATPase module shows strong similarities to that in the clamped state. Notably, upon engagement, both SMC1A- and SMC3-HDs undergo lever effects that release them from their specific relaxed conformations (Figures 5D and 5E). In addition, engagement repositions the SMC1A F-loop, the SMC1A and SMC3 signature motifs, and the SMC3 wedge element and R-loop similarly as in the clamped state. Therefore, several of the structural rearrangements observed in the ATPase module in the clamped state are already occurring at the engagement stage.

However, despite these similarities, the structures of the engaged and clamped ATPase modules also show major differences. Notably, comparison of the heterodimerized ATPase modules reveals that whereas ATP binding is retained at both ATPase sites, the interaction between both HDs is tighter in the engaged complex than in the clamped complex. Specifically, the superposition of these complexes using the SMC1A-HD for fitting reveals a displacement by 2–3 Å of the SMC3-HD when comparing the engaged complex with the clamped complex (Figures 5F and S10A). Specifically, the central domain of NIPBL^{Scc2}, when bound to the SMC1A F-loop in the clamped state, is positioned at the interface between both HDs. Structural comparison shows that the accommodation of NIPBL^{Scc2} at this interface requires significant structural rearrangements, suggesting that the observed SMC3-HD displacement is due to steric hindrances caused upon NIPBL^{Scc2} binding.

This displacement does not cause loss of ATP at both ATPase sites and is enabled by significant changes within the complete SMC1A-HD/SMC3-HD interface, including the repositioning with respect to each other of the composite ATP-binding/hydrolysis motifs forming both sites. In the engaged complex, the positioning of these motifs appears to enable the SMC1A Q-loop Q137 side chain to adopt two different rotamer conformations, either turned toward the ATP molecule and the magnesium ion or toward the SMC1A E1157Q residue (Figure 5G). In the case of SMC3, while the Q141 side chain is now turned toward the ATPase site, the ATP γ-phosphate group appears imperfectly positioned to interact stably with this residue due to a void created between the ATP-binding motifs and within which the γ-phosphate of the bound ATP molecule can move (Figure 5H). These features could contribute to the moderate ATPase activity that we measured for the engaged ATPase module.

Figure 5. ATP-dependent engagement of the SMC1A- and SMC3-HDs yields an engaged ATPase module with a flexible SMC3-CC/RAD21N subcomplex

(A) Size exclusion chromatographic profiles and associated SDS-PAGE analyses of the mixed SMC1ACC-EQ/RAD21C and SMC3CC-EQ/RAD21N mutants in the absence (red) and the presence (orange) of ATP. All experiments were done in biological duplicate or triplicate. Asterisk, degradation products.

(B) Engagement analysis as in (A) using analytical ultracentrifugation velocity experiments. All experiments were done in biological duplicate.

(C) Structural model of the human engaged ATPase module displayed within the 3.6-Å resolution cryo-EM map.

(D) Superposition of the SMC1A-HDs of the engaged and clamped ATPase modules. In the clamped state, a stabilization of the upper region of the SMC1A CC that interacts with the C-terminal part of the hook domain of NIPBL^{Scc2} takes place.

(E) Superposition of the SMC3-HDs of the engaged and clamped ATPase modules. In the clamped state, a stabilization of the full SMC3-CC/RAD21N subcomplex that interacts with NIPBL^{Scc2} takes place.

(F) Superposition of the engaged and clamped ATPase modules using the SMC1A-HD as reference. For clarity, only the engaged SMC1A-HD and the region of NIPBL^{Scc2} (yellow) binding to the F-loop are displayed. See also Figure S10A.

(G) Representation of the ATP-binding motifs forming the SMC1A composite ATPase active site and of the bound ATP molecule and Mg ion displayed in the 3.6-Å cryo-EM map.

(H) Same as in (G) for the SMC3 composite ATPase site.

(I) Quantification of crosslinked species for the SMC3CC-D192C/RAD21N-K26C pair in experiments performed at room temperature. The supplementation of the SMC1ACC/RAD21C, ATP, and DNA is indicated below the graph. Experiments were done either with SMC1A- and SMC3-HDs harboring EQ mutants (left and center) or without EQ mutants (right). Experiments were also done using RAD21N deleted from its first 21 residues (center). The data are represented as mean ± SD. All measurements were made in technical or biological triplicate.

Engagement induces an oscillation of the SMC3-CC/RAD21N subcomplex

Our structural comparison between the engaged and clamped complexes also reveals major differences for the SMC1A and SMC3 CCs. In the case of the SMC1A-HD, three to five helical turns within each helix of its proximal CC are stabilized in the clamped complex; these are otherwise disordered in our cryo-EM map of the engaged ATPase module (Figure 5D). This stabilized region of the SMC1A CC is that interacting directly with $NIPBL^{Scc2}$ in the clamped complex. The difference is even larger in the case of the SMC3-HD since, in our cryo-EM map, there is an absence of density for the SMC3-CC/RAD21N subcomplex. Specifically, the density for the SMC3 CC is lost where this CC is kinked in our crystallographic structures (Figures 5C and 5E).

The absence of a resting state for the SMC3-CC/RAD21N subcomplex in the engaged ATPase module agrees with the fact that the lever effect is incompatible with the resting state of the SMC3-HD (Figure 4F). This suggests that engagement releases the resting state of the SMC3-HD through the repositioning of the SMC3 second signature-coupling helix upon leverage. This release of the resting state does not cause, however, a straightening of the SMC3 CC that would enable the SMC3-HD/RAD21N complex to adopt a conformation similar to that observed in the clamped state (Figure 5E), suggesting that the SMC3-CC/RAD21N subcomplex oscillates between these conformations.

To investigate this dynamic of the SMC3-CC/RAD21N subcomplex upon engagement, we have performed site-specific crosslinking experiments in solution between the SMC3 GD and RAD21N. Based on our structures and the structure of the clamped complex, we identified two pairs of residues in the SMC3 GD and in RAD21N (SMC3CC-D120/RAD21N-K25 and SMC3-D92/RAD21N-K26) that could be used for these experiments (Figures 4D and 4E). These residues, when mutated to cysteines, are well positioned for crosslinking with bis-maleimidoethane (BMOE) in a conformation close to the resting state (8.5 and 9.5 Å, respectively) but not in the clamped state (14.0 Å and 25.0 Å, respectively).

Crosslinking experiments with the SMC3CC-D120C (EQ mutant)/RAD21N-K25C complex gave a robust crosslinking (>40%–50%; Figures S11A–S11D). The amounts of crosslink were, however, not significantly modified in the presence of SMC1A (EQ mutant) alone, with ATP, or with ATP and DNA. We reasoned that this could be due to the insufficient amplitude of the oscillation of the SMC3-CC/RAD21N subcomplex (maximal distance of 14 Å) that keeps the cysteine residues at crosslinking distance. Accordingly, using the SMC3CC-D92C (EQ mutant)/RAD21N-K26C complex, where the distance between the crosslinking residues increases more rapidly upon oscillation (maximal distance of 25.0 Å), significant differences in crosslinking were observed. Notably, lower amounts of crosslinked species were initially observed that increased with time, but only in the presence of SMC1A (EQ mutant) supplemented with either ATP or ATP and DNA (Figures 5I, S11A, S11B, S11E, and S11F). This suggested that loss of crosslinking only occurs when the resting state of the SMC3-HD/RAD21N complex is lost upon engagement.

We confirmed this hypothesis by using a SMC3-HD/RAD21N complex impaired in forming the resting state upon deletion of the 21 first residues of RAD21N. In this case, a reduction of the crosslink amounts was already observed for the SMC3-HD/RAD21N complex alone, and these amounts did not increase significantly with time (Figure 5I). Crosslinking was also performed using SMC1A- and SMC3-HDs that do not harbor EQ mutations, enabling ATP hydrolysis, disengagement, and resting state formation several times between our measurement time points. In this case, the crosslink amounts were slightly increased in all conditions and the reduction in crosslink amounts as well as their time dependence in the presence of SMC1A and ATP disappeared (Figure 5I). Collectively, our crosslinking results agree with a release of the resting state of the SMC3-HD/RAD21N complex upon engagement with a subsequent oscillation of the SMC3-CC/RAD21N subcomplex.

Opening of the SMC3-HD/RAD21N interface keeps engagement but stiffens the SMC3 CC and positions the SMC1A and SMC3 CCs in the ATPase module DNA-binding chamber

We then used our 4.4-Å resolution cryo-EM map for model building. This map showed density for the SMC3 CC emerging from the SMC3 GD but not for RAD21N. We fitted our 3.6-Å resolution engaged ATPase module structure into this map, added the SMC3 CC, and performed cycles of main chain manual modification and automatic real space refinement to obtain a structural model that enabled the identification of the positions of secondary structure elements (Figures 6A and S9; Table S5). Despite the medium resolution and a significant flexibility of the CCs, the modeling agreed with the presence of a structured SMC3 CC but not of RAD21N. Due to the lack of RAD21N, we termed open-engaged this second complex of the human ATPase module. Structural comparison showed that our human open-engaged complex is similar to the yeast ATPase module lacking Scc1N, where the Smc3 CC also adopts a stable conformation, thus confirming our observations.[13]

Comparison of our engaged and open-engaged complexes revealed major differences. Notably, both lever effects are lost in the open-engaged complex. Consequently, the SMC1A and SMC3 second signature helices make backward movements in the open-engaged complex compared to the engaged complex (Figures 6B and 6C). These movements are due to the back sliding of the SMC1A and SMC3 helical lobes with respect to their RecA lobes. In the case of SMC1A, the resulting open-engaged SMC1A-HD/RAD21C complex adopts a structure similar to that of the non-engaged SMC1A-HD/RAD21C complex in its relaxed state when bound to ATPγS (Figure 6D). In this conformation, the rotational movement of the SMC1A CC from its central position, observed in the apo and the engaged/clamped structures of the SMC1A-HD, toward the RecA lobe moves this CC toward the ATPase module DNA-binding chamber.

In the case of the open-engaged SMC3-HD, its GD also adopts a relaxed conformation similar to that observed in the isolated SMC3-HD/RAD21N complex (Figure 6E). However, the open-engaged SMC3 CC does not adopt a resting state conformation. Rather, upon the loss of RAD21N, the SMC3 CC emerging from the SMC3 GD is locked in a stiff conformation and makes an ~90° angle compared to that in the resting state

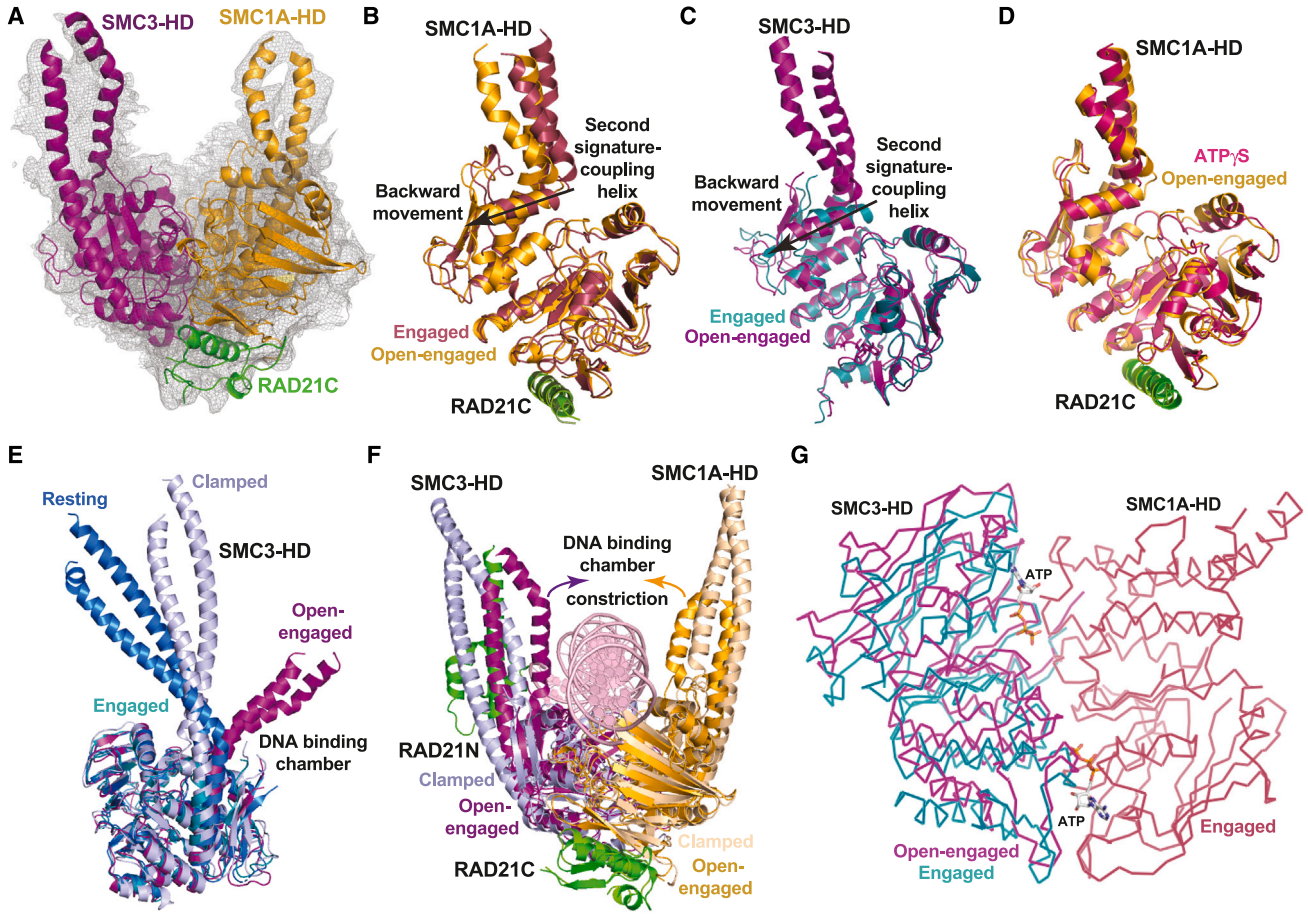

Figure 6. Opening of the SMC3-CC/RAD21N interface keeps the ATP gate shut but causes the stiffening of the SMC3 CC that constricts the DNA-binding chamber of the cohesin ATPase module

(A) Structural model of the human open-engaged ATPase module displayed within the 4.4-Å resolution cryo-EM map.

(B) Superposition of the SMC1A-HDs of the engaged and open-engaged ATPase modules.

(C) Same as in (B) for the engaged and open-engaged SMC3-HDs.

(D) Superposition of the open-engaged SMC1A-HD/RAD21C complex with the ATPγS-bound isolated SMC1A-HD/RAD21C complex.

(E) Structural superposition of the resting (blue), engaged (green-cyan), open-engaged (violet), and clamped (light blue) SMC3-HD structures. For clarity, RAD21N was removed, when applicable.

(F) Superposition of the clamped and open-engaged complexes showing the constriction of the DNA-binding chamber upon dissociation of the SMC3-HD/RAD21N interface. See also Figure S14.

(G) Superposition of the engaged and open-engaged ATPase modules using the SMC1A-HD as reference. For clarity, only the engaged SMC1A-HD is displayed. See also Figure S10B.

(Figure 6E). In this conformation, the open-engaged SMC3 CC is also repositioned into the ATPase module DNA-binding chamber. As such, the movements of both SMC1A and SMC3 proximal coiled coils in the open-engaged state constricts the ATPase module DNA-binding chamber (Figure 6F).

Despite the major structural rearrangements within both HDs, engagement is maintained in the absence of RAD21N. In addition, specific features observed upon engagement, such as the conformational rearrangement of the SMC3 wedge region and R-loop, are kept in the open-engaged ATPase module. However, to keep engagement, a major reorganization of the SMC1A-HD/SMC3-HD interface occurs that is even larger than the one observed between the engaged and clamped ATPase modules (Figures 6G and S10B). This reorganization appears to further offset the ATP-binding/hydrolysis motifs with respect to each other.

The SMC3-HD/RAD21N interface including its RAD21N HeID domain are functionally important in vertebrates

Our different results have suggested an important role for the full N-terminal domain of RAD21 during the human cohesin ATPase cycle. Whereas the functional importance of the long RAD21N α helix that binds to the SMC3 CC and enables the formation of the SMC3-HD/RAD21 interface has already been demonstrated, less is known about the functional importance of the RAD21N HeID domain. Sequence comparison shows that this domain is

highly conserved in vertebrates (99% sequence identity) (Figure S3), suggesting that the role of the RAD21N HelD is conserved in these organisms.

To assess the functional importance of the RAD21N HelD region in vertebrates, we obtained a characterized *rad21a* zebrafish mutant line,[58] which we used to evaluate the effect of truncating various parts of the RAD21N region. Homozygous mutant larvae exhibited microcephaly, large pericardial edema, and curved bodies at 3 days post-fertilization (dpf), which mirrored clinical features of the CdLS (Figures 7A and S12).[59] These phenotypes were specific and could be rescued efficiently upon injection of 200 pg WT zebrafish full-length *rad21a* mRNA (Figures 7A–7C and S12).

To test the requirement of the RAD21 HelD domain in cohesin function, and notably of its N-terminal helix that enables the resting state conformation of the SMC3-HD, we injected a mutant mRNA that did not code for the first 21 amino acids of RAD21 (RAD21-Δ21) into homozygous mutant eggs. The RAD21-Δ21 mRNA failed to rescue the *rad21a*$^{-/-}$ phenotypes compared to the WT mRNA (Figures 7B, 7C, and S12). Specifically, body curvature, eye diameter (as a readout for microcephaly), and pericardial edema of RAD21-Δ21-injected larvae were affected indistinguishably from non-injected rad21a homozygous mutant larvae, suggesting that RAD21-Δ21 acts as a loss-of-function allele. The loss of rescue observed with the RAD21-Δ21 mRNA indicated that the absence of the first 21 residues induces a loss of function of *rad21a*, thus confirming the critical role of the RAD21 HelD domain for cohesin function in vertebrates.

We made a comparative analysis with a *rad21a* mRNA lacking the full RAD21N region (RAD21-Δ87). This mutant, which should prevent the formation of a functional cohesin complex *in vivo* by destroying the SMC3-HD/RAD21N interface, led to an aggravated phenotype rather than a rescued phenotype, as shown by the gross observation of dead tissue in the head of homozygous mutant embryos at 1 dpf, and developmental arrest. Similarly, injection of the zebrafish RAD21-Δ87 mRNA into WT eggs led to the same severe phenotype. The presence of dead cells was confirmed by acridine orange staining of RAD21-Δ87 mRNA-injected embryos (Figure S12E). Accordingly, TUNEL staining revealed a significant increase in the number of apoptotic cells in the head compared to control embryos or embryos injected with WT *rad21a* mRNA (Figure 7D).

To determine whether the RAD21-Δ87 mutant acts as a dominant negative or a gain of function, we injected into WT eggs an mRNA coding either for the RAD21-Δ87 alone or in combination with an mRNA coding for the WT protein. Our data showed that the phenotype induced by the RAD21-Δ87 mutant can be significantly rescued by the addition of WT mRNA, confirming that this mutant is dominant negative (Figure S12F). Altogether, these *in vivo* data suggest the essential function of RAD21N in vertebrates, including its N-terminal HelD domain.

DISCUSSION

The molecular mechanisms underlying the ATPase activity of cohesin have remained poorly understood. Here, we show that the SMC1A- and SMC3-HDs undergo specific conformational movements along the cohesin ATPase cycle (Videos S1, S2, and S3). These movements are notably driven by the repositioning with respect to one another of the RecA lobe and helical lobe of each HD, enabling both HDs to switch between relaxed and engaged conformations. Nevertheless, many of our findings also unravel conformational movements that are specific to each HD, in agreement with their evolutionary divergence at the sequence, structural, and functional levels.

Differences are already observed upon nucleotide binding to the non-engaged HDs. This binding involves different thermodynamic contributions (entropic for SMC1A and enthalpic for SMC3) and cause specific rearrangements within both HDs. Specifically, in the case of the SMC1A-HD, this includes a repositioning of its proximal CC in a nucleotide binding-dependent manner that is linked to the movement of its two lobes with respect to each other. The proximal CC of the SMC1A-HD appears, however, conformationally stable throughout the ATPase cycle, as evidenced by our structural snapshots.

In contrast, the SMC3-HD proximal CC is little affected by nucleotide binding but displays an intrinsic flexibility at its base that enables it to adopt different conformations along the ATPase cycle. Specifically, prior to engagement, the SMC3-HD CC adopts a resting state through the interaction of the SMC3 GD and RAD21N. The ATP-dependent engagement of the SMC1A- and SMC3-HDs to form the ATPase module causes both HDs to move from their relaxed to their engaged conformations, which, in turn, forces the release of the resting state of the SMC3-HD CC that becomes flexible. Upon opening of the SMC3-HD/RAD21N interface, the SMC3-HD CC is stabilized but adopts a specific conformation 90° away from that in the resting state.

The flexibility of the SMC3-HD CC upon engagement suggests that to form the clamped state, an important role of NIPBL^{Scc2} is to stabilize this CC. However, any intermediate conformation between the resting and clamped states of the SMC3-HD CC is sterically incompatible with the position of the NIPBL^{Scc2} nose in the clamped state (Figure S13A). This suggests that the formation of the clamped complex requires a conjoint movement of the SMC3-CC/RAD21N subcomplex and of the NIPBL^{Scc2} nose (Video S3).

Another consequence of engagement is the repositioning and conformational rearrangement of the F-loop that should favor docking of NIPBL^{Scc2}. Although this docking could take place after the ATP-dependent engagement of the SMC1A- and SMC3-HDs, it has been proposed that NIPBL^{Scc2} bound to DNA first interacts with the non-engaged SMC3-HD prior to engagement of both HDs.[51] The relaxed conformation of the non-engaged SMC3-HD, including the resting state of the SMC3-CC/RAD21N subcomplex, which displays a positively charged electrostatic patch different from that observed in the clamped state (Figures S13B and S13C), could serve as the specific docking platform for the incoming NIPBL^{Scc2}/DNA complex. Subsequent engagement with the oscillation of the SMC3-CC/RAD21N subcomplex and the rearrangement of the F-loop could then facilitate the interaction of NIPBL^{Scc2} with the SMC1A-HD to form the clamped complex.

In the clamped state, the DNA lies on the positively charged pit formed by the engaged SMC1A and SMC3 GDs, the SMC1A and

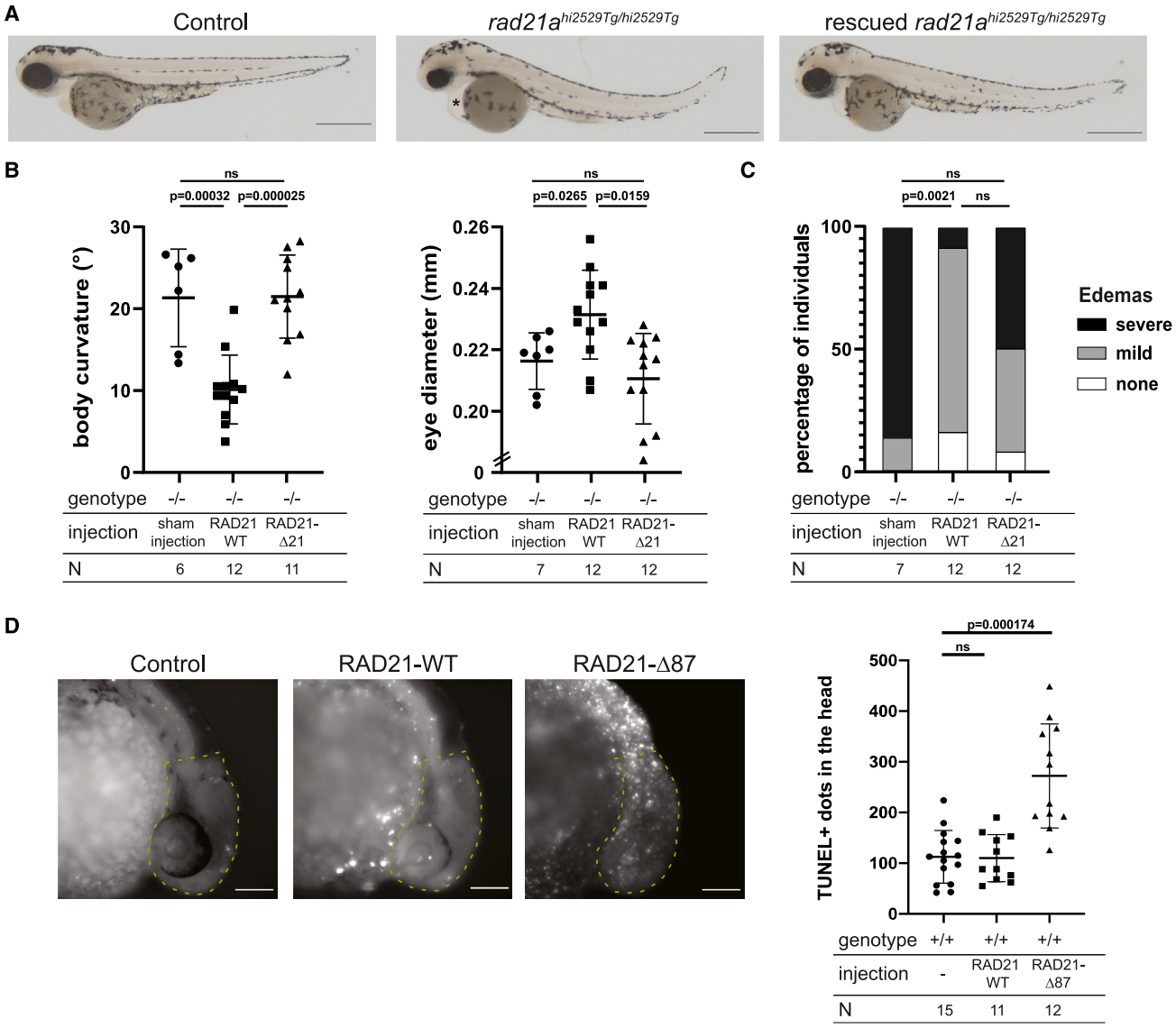

Figure 7. Functional importance of the RAD21N HelD domain and of the SMC3-HD/RAD21N interface in the zebrafish

(A) From left to right, representative lateral images of zebrafish control *rad21a*$^{+/+}$, homozygous mutant *rad21a*$^{hi2529Tg/hi2529Tg}$, and homozygous mutant *rad21a*$^{hi2529Tg/hi2529Tg}$ larvae rescued with 200 pg mRNA encoding WT full-length *Danio rerio rad21a* at 3 dpf. Scale bar, 0.5 mm. Asterisk indicates the presence of a pericardial edema.

(B) Dot plots of the measurements of body curvature (degrees) and eye diameter (millimeters) for homozygous mutant *rad21a*$^{hi2529Tg/hi2529Tg}$ larvae injected with sham or full-length WT *D. rerio rad21a* (RAD21 WT) or with the *rad21a* mRNA lacking the first 21 residues (RAD21-Δ21). Statistical significance was assessed by ANOVA followed by a Tukey's test for post hoc analysis. All experiments were done in biological duplicate. The *p* values are indicated on the graphs. N corresponds to the number of embryos per condition.

(C) Bar graph showing the presence of pericardial edema for homozygous mutant *rad21a*$^{hi2529Tg/hi2529Tg}$ larvae injected with sham or full-length WT *D. rerio rad21a* (RAD21 WT) or with the *rad21a* mRNA lacking the first 21 residues (RAD21-Δ21). Larvae were binned into three categories: severe, mild, or absent (none). Statistical significance was assessed by a Fisher's exact test. All experiments were done in biological duplicate. The *p* values are indicated on the graphs. N corresponds to the number of embryos per condition.

(D) From left to right, representative lateral images of uninjected WT larvae (shown as Control) and WT larvae injected at 1 dpf with either full-length WT *D. rerio rad21a* (RAD21 WT) or a *rad21a* mRNA that do not code for the first 87 residues (RAD21-Δ87). The dot plot represents the number of TUNEL+ dots in the highlighted brain area (dotted line on the images) for the three conditions. A t test was conducted between pairs of conditions to determine significance. The *p* values are indicated on the graphs. The TUNEL experiments were done in biological duplicate. N corresponds to the number of embryos per condition. Scale bar, 0.1 mm; ns, non-significant.

SMC3 proximal CCs forming the walls of the DNA-binding chamber (Figure S13D).[10–12] Whereas the SMC3 CC and the RAD21N HelD display a high positive charge that contributes to the electrostatic binding of the DNA, the SMC1A CC shows no strong electrostatic potential and appears mainly to act as a rigid wall to keep the DNA in its binding chamber.

Upon engagement, the oscillation of the SMC3 CC/RAD21N subcomplex is expected to cause a widening of the DNA-binding chamber that should facilitate DNA entry and positioning into this chamber (Figure S13E). Notably, the specific conformational rearrangements of the SMC1A- and SMC3-HDs upon engagement are concerted and enable the formation of the DNA-binding chamber (Video S3). In the clamped state the DNA is also responsible for the correct positioning of the NIPBL^{Scc2} nose, suggesting that the DNA is an actor of its own entrapment.

Dissociation of RAD21N from the ATPase module has a stabilizing effect for the SMC3 CC that becomes positioned within the DNA-binding chamber of the ATPase module. RAD21N loss also causes both SMC1A- and SMC3-HDs to come back to their relaxed conformation, which also moves the SMC1A CC toward the DNA-binding chamber. The resulting chamber displays a reduced positive charge (Figure S13F) and is constricted due to the positioning of the SMC1A and SMC3 CCs. This constriction is poorly compatible with DNA binding (Video S3). Importantly, the fitting of our human open-engaged structure within the cryo-EM map of the full-length ATP-engaged *S. cerevisiae* core cohesin complex lacking Scc1 (EMBD: EMD-12889) reveals that the conformation of the open-engaged SMC3 CC agrees relatively well with the cryo-EM density, in contrast to its resting and clamped state conformations (Figure S14).

The yeast complex lacking Scc1 forms a compact and overall rigid structure compared to other structures published.[10–12,14] The SMC3-HD/RAD21N interface has been called the DNA exit gate and its opening shown to allow the release of a topologically entrapped DNA from the cohesin ring.[20,26,28,37,39,41] Specifically, entrapment of DNA has been shown to occur in the kleisin compartment rather than in the SMC compartment.[53] Opening of the SMC3-HD/RAD21N interface could therefore cause the release of the entrapped DNA, also forcing the SMC heterodimer to adopt a tight conformation that is less prone to interactions with DNA but also with NIPBL^{Scc2} due to the relaxed conformation of the SMC1A-HD.

Our analyses have highlighted the importance of RAD21N, including its HelD, for the specific conformational dynamics of the SMC3-HD and cohesin ATPase module. Our *in vivo* experiments in zebrafish confirm that RAD21N and its HelD domain are functionally important, including the first 21 residues of RAD21 that interact with the SMC3 GD in the resting state of the SMC3-HD/RAD21N complex (Figure S15A). Previous work also suggested a role for the first 20 amino acids of RAD21 in its interplay with PDS5 and WAPL.[31] The HelD domain is also involved in the formation of the clamped state, both in human and in *Schizosaccharomyces pombe* (Figures S15B and S15C).[10,12] Curiously, the HelD domain is less structured in *S. cerevisiae* (Figures S15D and S15E).[6,11] This suggests that the Smc3-HD/Scc1N complex could be less prone to adopt a resting state. Interestingly, in the paralogous condensin complex, a HelD is also present in the CAP-H^{Brn1} kleisin, and current structural data suggest that it could also play a similar role to that of cohesin during the condensin ATPase cycle.[60–63]

Finally, our study reveals the high plasticity of the ATP interface between the SMC1A- and SMC3-HDs that enables these HDs to remain engaged while undergoing major structural rearrangements. Specifically, in comparison to the engaged state, NIPBL^{Scc2} binding or loss of RAD21N cause important and distinct reorganizations of the ATPase module and of the SMC1A-HD/SMC3-HD interface without, however, causing the opening of the ATP gate. The modular nature of both ATP-binding sites, which are formed by small motifs whose positioning relative to one another can be varied, appears essential to allow this plasticity, potentially providing a way of regulating the cohesin ATPase activity. In contrast, the hydrolysis of ATP into ADP cannot support engagement, highlighting the importance of the ATP γ-phosphate to keep the heterodimeric engagement of both HDs. As such, our results suggest that the ATP gate can be kept closed in a low ATPase activity conformation through specific regulatory mechanisms. In this respect, the cohesin ATPase cycle can be divided in two potentially independent steps: an ATP-dependent engagement with formation of the ATP gate and an ATP hydrolysis-dependent disengagement causing the opening of the ATP gate.

Limitations of the study

The conclusions drawn from our structural analyses may have been impacted by the influence of crystal packing and cryo-EM sample preparation as well as the resolution obtained for some structures. In addition, to study in precise molecular terms the conformational dynamic of the cohesin SMC1A- and SMC3-HDs during the ATPase cycle, our work has focused on the isolated SMC1A- and SMC3-HDs and cohesin ATPase module. Our study has therefore left aside the analysis of the influence of the cohesin arms and of the numerous cohesin regulators, including NIPBL, on this cycle, which remain to be investigated.

RESOURCE AVAILABILITY

Lead contact

Further information and requests for resources and reagents should be directed to and will be fulfilled by the lead contact, Christophe Romier (romier@igbmc.fr).

Materials availability

All unique/stable newly generated materials associated with this paper will be made available by the lead author upon request after establishment of a Material Transfer Agreement.

Data and code availability

- The crystallographic and cryo-EM structures reported in this manuscript have been deposited in the PDB and are publicly available from the date of publication (PDB: 8ro6, 8ro7, 8ro8, 8ro9, 8roa, 8rob, 8roc, 8rod, 8roe, 8rof, 8rog, 8roh, 8roi, 8roj, 8rok, 8rol, 8p0a, 8pq5). Data reported in this manuscript will be shared by the lead contact upon request.
- This paper does not report original code.
- Any additional information required to reanalyse the data reported in this work paper is available from the lead contact upon request.

ACKNOWLEDGMENTS

We thank Catherine Birck, Gaëlle Hayot, Nils Marechal, Alastair McEwen, Gabor Papai, Pierre Poussin-Courmontagne, Helgo Schmidt, Piotr Sosnowski, and Albert Weixlbaumer from the IGBMC for their help during data collection and data analysis. We thank the Zebrafish International Resource Center (Eugene, OR) for providing the zebrafish line used and the IGBMC Zebrafish Facility, in particular Sandrine Geschier, for maintenance and care of the zebrafish line. We thank members of the SOLEIL and SLS synchrotrons for the use of their beamline facilities and help during data collection. This work of the Interdisciplinary Thematic Institute IMCBio+, as part of the ITI 2021–2028 program of the University of Strasbourg, Centre National de la Recherche Scientifique (CNRS), and Institut National de la Santé et de la Recherche Médicale (INSERM), was supported by the INRT LabEx (ANR-10-LABX-030-INRT), IdEx Unistra (ANR-10-IDEX-0002), SFRI-STRAT'US project (ANR-20-SFRI-0012), and EUR IMCBio (ANR-17-EURE-0023) under the framework of the France 2030 Program. The cryo-electron microscope Glacios was co-financed by the European Union, with the European Regional Development Fund, the Strasbourg Eurometropole, and the French Infrastructure for Integrated Structural Biology (FRISBI; ANR-10-INBS-0005-01). This work was supported by the Agence Nationale de la Recherche (ANR-17-CE12-0006, ANR-21-CE12-0026, ANR-23-CE11-0019), the Fondation Association pour la Recherche sur le Cancer (ARCPJA20181208268, ARCPJA2021060003715, DOC20180507150), the Fondation pour la Recherche Médicale (FDT202106012973), and institutional funds from the CNRS, INSERM, and University of Strasbourg.

AUTHOR CONTRIBUTIONS

M.V.G., P.L., T.B.S., E.T., C.D., and M.-L.D.-D. made the clones and purified the proteins. M.V.G. and P.L. performed the ATPase assays. M.-L.D.-D. and M.V.G. performed the crosslinking experiments. K.B. and E.E. collected the ITC data. M.V.G., T.B.S., and C.R. performed the crystallographic analyses. P.L., A.D., C.R., and M.-L.D.-D. performed the cryo-EM analyses. M.-L.D.-D., C.W., L.D., M.V.L., and C.G. performed the zebrafish analyses. M.V.G., P.L., M.-L.D.-D., T.B.S., A.D., E.E., C.G., and C.R. planned the experiments. All authors analyzed and discussed the data. C.R. wrote the manuscript, and all authors commented on the manuscript.

DECLARATION OF INTERESTS

The authors declare no competing interests.

STAR★METHODS

Detailed methods are provided in the online version of this paper and include the following:

- KEY RESOURCES TABLE
- EXPERIMENTAL MODEL AND STUDY PARTICIPANT DETAILS
- METHOD DETAILS
  - Cloning
  - Protein complexes production and purification
  - ATPase assays
  - Isothermal titration calorimetry measurements
  - Crystallizations
  - Crystallographic structure determination, model building and refinement
  - Reconstitution of the ATP-engaged ATPase module by size exclusion chromatography
  - Reconstitution of the ATP-engaged ATPase module by analytical ultracentrifugation (AUC) experiments
  - Cryo-electron microscopy sample preparation and data acquisition
  - Cryo-electron microscopy data processing, model building and refinement
  - Cross-linking experiments
  - Zebrafish mutant line, *in vivo* complementation experiments and whole-mount immunostaining
  - Structural data
  - Generation of the graphical supports
- QUANTIFICATION AND STATISTICAL ANALYSIS

SUPPLEMENTAL INFORMATION

Supplemental information can be found online at https://doi.org/10.1016/j.celrep.2024.114656.

A video abstract is available at https://doi.org/10.1016/j.celrep.2024.114656#mmc5.

Received: December 15, 2023
Revised: June 17, 2024
Accepted: August 2, 2024

REFERENCES

1. Davidson, I.F., and Peters, J.M. (2021). Genome folding through loop extrusion by SMC complexes. Nat. Rev. Mol. Cell Biol. *22*, 445–464. https://doi.org/10.1038/s41580-021-00349-7.
2. Haering, C.H., and Gruber, S. (2016). Snapshot: SMC protein complexes Part I. Cell *164*, 326–326.e1. https://doi.org/10.1016/j.cell.2015.12.026.
3. Yatskevich, S., Rhodes, J., and Nasmyth, K. (2019). Organization of Chromosomal DNA by SMC Complexes. Annu. Rev. Genet. *53*, 445–482. https://doi.org/10.1146/annurev-genet-112618-043633.
4. Gligoris, T., and Löwe, J. (2016). Structural Insights into Ring Formation of Cohesin and Related Smc Complexes. Trends Cell Biol. *26*, 680–693. https://doi.org/10.1016/j.tcb.2016.04.002.
5. Hopfner, K.P., and Tainer, J.A. (2003). Rad50/SMC proteins and ABC transporters: unifying concepts from high-resolution structures. Curr. Opin. Struct. Biol. *13*, 249–255. https://doi.org/10.1016/s0959-440x(03)00037-x.
6. Gligoris, T.G., Scheinost, J.C., Bürmann, F., Petela, N., Chan, K.L., Uluocak, P., Beckouët, F., Gruber, S., Nasmyth, K., and Löwe, J. (2014). Closing the cohesin ring: structure and function of its Smc3-kleisin interface. Science *346*, 963–967. https://doi.org/10.1126/science.1256917.
7. Haering, C.H., Löwe, J., Hochwagen, A., and Nasmyth, K. (2002). Molecular architecture of SMC proteins and the yeast cohesin complex. Mol. Cell *9*, 773–788. https://doi.org/10.1016/s1097-2765(02)00515-4.
8. Haering, C.H., Schoffnegger, D., Nishino, T., Helmhart, W., Nasmyth, K., and Löwe, J. (2004). Structure and stability of cohesin's Smc1-kleisin interaction. Mol. Cell *15*, 951–964. https://doi.org/10.1016/j.molcel.2004.08.030.
9. Kurze, A., Michie, K.A., Dixon, S.E., Mishra, A., Itoh, T., Khalid, S., Strmecki, L., Shirahige, K., Haering, C.H., Löwe, J., and Nasmyth, K. (2011). A positively charged channel within the Smc1/Smc3 hinge required for sister chromatid cohesion. EMBO J. *30*, 364–378. https://doi.org/10.1038/emboj.2010.315.
10. Shi, Z., Gao, H., Bai, X.C., and Yu, H. (2020). Cryo-EM structure of the human cohesin-NIPBL-DNA complex. Science *368*, 1454–1459. https://doi.org/10.1126/science.abb0981.
11. Collier, J.E., Lee, B.G., Roig, M.B., Yatskevich, S., Petela, N.J., Metson, J., Voulgaris, M., Gonzalez Llamazares, A., Löwe, J., and Nasmyth, K.A. (2020). Transport of DNA within cohesin involves clamping on top of engaged heads by Scc2 and entrapment within the ring by Scc3. Elife *9*, e59560. https://doi.org/10.7554/eLife.59560.
12. Higashi, T.L., Eickhoff, P., Sousa, J.S., Locke, J., Nans, A., Flynn, H.R., Snijders, A.P., Papageorgiou, G., O'Reilly, N., Chen, Z.A., et al. (2020). A Structure-Based Mechanism for DNA Entry into the Cohesin Ring. Mol. Cell *79*, 917–933.e9. https://doi.org/10.1016/j.molcel.2020.07.013.

13. Muir, K.W., Li, Y., Weis, F., and Panne, D. (2020). The structure of the cohesin ATPase elucidates the mechanism of SMC-kleisin ring opening. Nat. Struct. Mol. Biol. *27*, 233–239. https://doi.org/10.1038/s41594-020-0379-7.

14. Petela, N.J., Gonzalez Llamazares, A., Dixon, S., Hu, B., Lee, B.G., Metson, J., Seo, H., Ferrer-Harding, A., Voulgaris, M., Gligoris, T., et al. (2021). Folding of cohesin's coiled coil is important for Scc2/4-induced association with chromosomes. Elife *10*, e67268. https://doi.org/10.7554/eLife.67268.

15. Davidson, I.F., Bauer, B., Goetz, D., Tang, W., Wutz, G., and Peters, J.M. (2019). DNA loop extrusion by human cohesin. Science *366*, 1338–1345. https://doi.org/10.1126/science.aaz3418.

16. Kim, Y., Shi, Z., Zhang, H., Finkelstein, I.J., and Yu, H. (2019). Human cohesin compacts DNA by loop extrusion. Science *366*, 1345–1349. https://doi.org/10.1126/science.aaz4475.

17. Murayama, Y., and Uhlmann, F. (2014). Biochemical reconstitution of topological DNA binding by the cohesin ring. Nature *505*, 367–371. https://doi.org/10.1038/nature12867.

18. Petela, N.J., Gligoris, T.G., Metson, J., Lee, B.G., Voulgaris, M., Hu, B., Kikuchi, S., Chapard, C., Chen, W., Rajendra, E., et al. (2018). Scc2 Is a Potent Activator of Cohesin's ATPase that Promotes Loading by Binding Scc1 without Pds5. Mol. Cell *70*, 1134–1148.e7. https://doi.org/10.1016/j.molcel.2018.05.022.

19. Arumugam, P., Gruber, S., Tanaka, K., Haering, C.H., Mechtler, K., and Nasmyth, K. (2003). ATP hydrolysis is required for cohesin's association with chromosomes. Curr. Biol. *13*, 1941–1953. https://doi.org/10.1016/j.cub.2003.10.036.

20. Buheitel, J., and Stemmann, O. (2013). Prophase pathway-dependent removal of cohesin from human chromosomes requires opening of the Smc3-Scc1 gate. EMBO J. *32*, 666–676. https://doi.org/10.1038/emboj.2013.7.

21. Gruber, S., Arumugam, P., Katou, Y., Kuglitsch, D., Helmhart, W., Shirahige, K., and Nasmyth, K. (2006). Evidence that loading of cohesin onto chromosomes involves opening of its SMC hinge. Cell *127*, 523–537. https://doi.org/10.1016/j.cell.2006.08.048.

22. Haering, C.H., Farcas, A.M., Arumugam, P., Metson, J., and Nasmyth, K. (2008). The cohesin ring concatenates sister DNA molecules. Nature *454*, 297–301. https://doi.org/10.1038/nature07098.

23. Hu, B., Itoh, T., Mishra, A., Katoh, Y., Chan, K.L., Upcher, W., Godlee, C., Roig, M.B., Shirahige, K., and Nasmyth, K. (2011). ATP hydrolysis is required for relocating cohesin from sites occupied by its Scc2/4 loading complex. Curr. Biol. *21*, 12–24. https://doi.org/10.1016/j.cub.2010.12.004.

24. Ladurner, R., Bhaskara, V., Huis in 't Veld, P.J., Davidson, I.F., Kreidl, E., Petzold, G., and Peters, J.M. (2014). Cohesin's ATPase activity couples cohesin loading onto DNA with Smc3 acetylation. Curr. Biol. *24*, 2228–2237. https://doi.org/10.1016/j.cub.2014.08.011.

25. Srinivasan, M., Scheinost, J.C., Petela, N.J., Gligoris, T.G., Wissler, M., Ogushi, S., Collier, J.E., Voulgaris, M., Kurze, A., Chan, K.L., et al. (2018). The Cohesin Ring Uses Its Hinge to Organize DNA Using Non-topological as well as Topological Mechanisms. Cell *173*, 1508–1519.e18. https://doi.org/10.1016/j.cell.2018.04.015.

26. Beckouet, F., Srinivasan, M., Roig, M.B., Chan, K.L., Scheinost, J.C., Batty, P., Hu, B., Petela, N., Gligoris, T., Smith, A.C., et al. (2016). Releasing Activity Disengages Cohesin's Smc3/Scc1 Interface in a Process Blocked by Acetylation. Mol. Cell *61*, 563–574. https://doi.org/10.1016/j.molcel.2016.01.026.

27. Chan, K.L., Gligoris, T., Upcher, W., Kato, Y., Shirahige, K., Nasmyth, K., and Beckouët, F. (2013). Pds5 promotes and protects cohesin acetylation. Proc. Natl. Acad. Sci. USA *110*, 13020–13025. https://doi.org/10.1073/pnas.1306900110.

28. Chan, K.L., Roig, M.B., Hu, B., Beckouët, F., Metson, J., and Nasmyth, K. (2012). Cohesin's DNA exit gate is distinct from its entrance gate and is regulated by acetylation. Cell *150*, 961–974. https://doi.org/10.1016/j.cell.2012.07.028.

29. Ladurner, R., Kreidl, E., Ivanov, M.P., Ekker, H., Idarraga-Amado, M.H., Busslinger, G.A., Wutz, G., Cisneros, D.A., and Peters, J.M. (2016). Sororin actively maintains sister chromatid cohesion. EMBO J. *35*, 635–653. https://doi.org/10.15252/embj.201592532.

30. Nishiyama, T., Ladurner, R., Schmitz, J., Kreidl, E., Schleiffer, A., Bhaskara, V., Bando, M., Shirahige, K., Hyman, A.A., Mechtler, K., and Peters, J.M. (2010). Sororin mediates sister chromatid cohesion by antagonizing Wapl. Cell *143*, 737–749. https://doi.org/10.1016/j.cell.2010.10.031.

31. Ouyang, Z., Zheng, G., Tomchick, D.R., Luo, X., and Yu, H. (2016). Structural Basis and IP6 Requirement for Pds5-Dependent Cohesin Dynamics. Mol. Cell *62*, 248–259. https://doi.org/10.1016/j.molcel.2016.02.033.

32. Rolef Ben-Shahar, T., Heeger, S., Lehane, C., East, P., Flynn, H., Skehel, M., and Uhlmann, F. (2008). Eco1-dependent cohesin acetylation during establishment of sister chromatid cohesion. Science *321*, 563–566. https://doi.org/10.1126/science.1157774.

33. Rowland, B.D., Roig, M.B., Nishino, T., Kurze, A., Uluocak, P., Mishra, A., Beckouët, F., Underwood, P., Metson, J., Imre, R., et al. (2009). Building sister chromatid cohesion: smc3 acetylation counteracts an antiestablishment activity. Mol. Cell *33*, 763–774. https://doi.org/10.1016/j.molcel.2009.02.028.

34. Unal, E., Heidinger-Pauli, J.M., Kim, W., Guacci, V., Onn, I., Gygi, S.P., and Koshland, D.E. (2008). A molecular determinant for the establishment of sister chromatid cohesion. Science *321*, 566–569. https://doi.org/10.1126/science.1157880.

35. Zhang, J., Shi, X., Li, Y., Kim, B.J., Jia, J., Huang, Z., Yang, T., Fu, X., Jung, S.Y., Wang, Y., et al. (2008). Acetylation of Smc3 by Eco1 is required for S phase sister chromatid cohesion in both human and yeast. Mol. Cell *31*, 143–151. https://doi.org/10.1016/j.molcel.2008.06.006.

36. Bernard, P., Schmidt, C.K., Vaur, S., Dheur, S., Drogat, J., Genier, S., Ekwall, K., Uhlmann, F., and Javerzat, J.P. (2008). Cell-cycle regulation of cohesin stability along fission yeast chromosomes. EMBO J. *27*, 111–121. https://doi.org/10.1038/sj.emboj.7601955.

37. Eichinger, C.S., Kurze, A., Oliveira, R.A., and Nasmyth, K. (2013). Disengaging the Smc3/kleisin interface releases cohesin from Drosophila chromosomes during interphase and mitosis. EMBO J. *32*, 656–665. https://doi.org/10.1038/emboj.2012.346.

38. Gandhi, R., Gillespie, P.J., and Hirano, T. (2006). Human Wapl is a cohesin-binding protein that promotes sister-chromatid resolution in mitotic prophase. Curr. Biol. *16*, 2406–2417. https://doi.org/10.1016/j.cub.2006.10.061.

39. Huis in 't Veld, P.J., Herzog, F., Ladurner, R., Davidson, I.F., Piric, S., Kreidl, E., Bhaskara, V., Aebersold, R., and Peters, J.M. (2014). Characterization of a DNA exit gate in the human cohesin ring. Science *346*, 968–972. https://doi.org/10.1126/science.1256904.

40. Kueng, S., Hegemann, B., Peters, B.H., Lipp, J.J., Schleiffer, A., Mechtler, K., and Peters, J.M. (2006). Wapl controls the dynamic association of cohesin with chromatin. Cell *127*, 955–967. https://doi.org/10.1016/j.cell.2006.09.040.

41. Murayama, Y., and Uhlmann, F. (2015). DNA Entry into and Exit out of the Cohesin Ring by an Interlocking Gate Mechanism. Cell *163*, 1628–1640. https://doi.org/10.1016/j.cell.2015.11.030.

42. Sutani, T., Kawaguchi, T., Kanno, R., Itoh, T., and Shirahige, K. (2009). Budding yeast Wpl1(Rad61)-Pds5 complex counteracts sister chromatid cohesion-establishing reaction. Curr. Biol. *19*, 492–497. https://doi.org/10.1016/j.cub.2009.01.062.

43. Tedeschi, A., Wutz, G., Huet, S., Jaritz, M., Wuensche, A., Schirghuber, E., Davidson, I.F., Tang, W., Cisneros, D.A., Bhaskara, V., et al. (2013). Wapl is an essential regulator of chromatin structure and chromosome segregation. Nature *501*, 564–568. https://doi.org/10.1038/nature12471.

44. Dauban, L., Montagne, R., Thierry, A., Lazar-Stefanita, L., Bastié, N., Gadal, O., Cournac, A., Koszul, R., and Beckouët, F. (2020). Regulation of

Cohesin-Mediated Chromosome Folding by Eco1 and Other Partners. Mol. Cell *77*, 1279–1293.e4. https://doi.org/10.1016/j.molcel.2020.01.019.

45. Haarhuis, J.H., and Rowland, B.D. (2017). Cohesin: building loops, but not compartments. EMBO J. *36*, 3549–3551. https://doi.org/10.15252/embj.201798654.
46. Li, Y., Haarhuis, J.H.I., Sedeño Cacciatore, Á., Oldenkamp, R., van Ruiten, M.S., Willems, L., Teunissen, H., Muir, K.W., de Wit, E., Rowland, B.D., and Panne, D. (2020). The structural basis for cohesin-CTCF-anchored loops. Nature *578*, 472–476. https://doi.org/10.1038/s41586-019-1910-z.
47. Nora, E.P., Caccianini, L., Fudenberg, G., So, K., Kameswaran, V., Nagle, A., Uebersohn, A., Hajj, B., Saux, A.L., Coulon, A., et al. (2020). Molecular basis of CTCF binding polarity in genome folding. Nat. Commun. *11*, 5612. https://doi.org/10.1038/s41467-020-19283-x.
48. Vian, L., Pękowska, A., Rao, S.S.P., Kieffer-Kwon, K.R., Jung, S., Baranello, L., Huang, S.C., El Khattabi, L., Dose, M., Pruett, N., et al. (2018). The Energetics and Physiological Impact of Cohesin Extrusion. Cell *175*, 292–294. https://doi.org/10.1016/j.cell.2018.09.002.
49. Wutz, G., Várnai, C., Nagasaka, K., Cisneros, D.A., Stocsits, R.R., Tang, W., Schoenfelder, S., Jessberger, G., Muhar, M., Hossain, M.J., et al. (2017). Topologically associating domains and chromatin loops depend on cohesin and are regulated by CTCF, WAPL, and PDS5 proteins. EMBO J. *36*, 3573–3599. https://doi.org/10.15252/embj.201798004.
50. Anderson, D.E., Losada, A., Erickson, H.P., and Hirano, T. (2002). Condensin and cohesin display different arm conformations with characteristic hinge angles. J. Cell Biol. *156*, 419–424. https://doi.org/10.1083/jcb.200111002.
51. Bauer, B.W., Davidson, I.F., Canena, D., Wutz, G., Tang, W., Litos, G., Horn, S., Hinterdorfer, P., and Peters, J.M. (2021). Cohesin mediates DNA loop extrusion by a "swing and clamp" mechanism. Cell *184*, 5448–5464.e22. https://doi.org/10.1016/j.cell.2021.09.016.
52. Bürmann, F., Lee, B.G., Than, T., Sinn, L., O'Reilly, F.J., Yatskevich, S., Rappsilber, J., Hu, B., Nasmyth, K., and Lowe, J. (2019). A folded conformation of MukBEF and cohesin. Nat. Struct. Mol. Biol. *26*, 227–236. https://doi.org/10.1038/s41594-019-0196-z.
53. Chapard, C., Jones, R., van Oepen, T., Scheinost, J.C., and Nasmyth, K. (2019). Sister DNA Entrapment between Juxtaposed Smc Heads and Kleisin of the Cohesin Complex. Mol. Cell *75*, 224–237.e5. https://doi.org/10.1016/j.molcel.2019.05.023.
54. Rohatgi, S., Clark, D., Kline, A.D., Jackson, L.G., Pie, J., Siu, V., Ramos, F.J., Krantz, I.D., and Deardorff, M.A. (2010). Facial diagnosis of mild and variant CdLS: Insights from a dysmorphologist survey. Am. J. Med. Genet. *152A*, 1641–1653. https://doi.org/10.1002/ajmg.a.33441.
55. Kamada, K., Su'etsugu, M., Takada, H., Miyata, M., and Hirano, T. (2017). Overall Shapes of the SMC-ScpAB Complex Are Determined by Balance between Constraint and Relaxation of Its Structural Parts. Structure *25*, 603–616. https://doi.org/10.1016/j.str.2017.02.008.
56. Camdere, G., Guacci, V., Stricklin, J., and Koshland, D. (2015). The ATPases of cohesin interface with regulators to modulate cohesin-mediated DNA tethering. Elife *4*, e11315. https://doi.org/10.7554/eLife.11315.
57. Elbatsh, A.M.O., Haarhuis, J.H.I., Petela, N., Chapard, C., Fish, A., Celie, P.H., Stadnik, M., Ristic, D., Wyman, C., Medema, R.H., et al. (2016). Cohesin Releases DNA through Asymmetric ATPase-Driven Ring Opening. Mol. Cell *61*, 575–588. https://doi.org/10.1016/j.molcel.2016.01.025.
58. Xu, B., Sowa, N., Cardenas, M.E., and Gerton, J.L. (2015). L-leucine partially rescues translational and developmental defects associated with zebrafish models of Cornelia de Lange syndrome. Hum. Mol. Genet. *24*, 1540–1555. https://doi.org/10.1093/hmg/ddu565.
59. Kline, A.D., Moss, J.F., Selicorni, A., Bisgaard, A.M., Deardorff, M.A., Gillett, P.M., Ishman, S.L., Kerr, L.M., Levin, A.V., Mulder, P.A., et al. (2018). Diagnosis and management of Cornelia de Lange syndrome: first international consensus statement. Nat. Rev. Genet. *19*, 649–666. https://doi.org/10.1038/s41576-018-0031-0.
60. Hassler, M., Shaltiel, I.A., Kschonsak, M., Simon, B., Merkel, F., Thärichen, L., Bailey, H.J., Macošek, J., Bravo, S., Metz, J., et al. (2019). Structural Basis of an Asymmetric Condensin ATPase Cycle. Mol. Cell *74*, 1175–1188.e9. https://doi.org/10.1016/j.molcel.2019.03.037.
61. Lee, B.G., Merkel, F., Allegretti, M., Hassler, M., Cawood, C., Lecomte, L., O'Reilly, F.J., Sinn, L.R., Gutierrez-Escribano, P., Kschonsak, M., et al. (2020). Cryo-EM structures of holo condensin reveal a subunit flip-flop mechanism. Nat. Struct. Mol. Biol. *27*, 743–751. https://doi.org/10.1038/s41594-020-0457-x.
62. Lee, B.G., Rhodes, J., and Löwe, J. (2022). Clamping of DNA shuts the condensin neck gate. Proc. Natl. Acad. Sci. USA *119*, e2120006119. https://doi.org/10.1073/pnas.2120006119.
63. Shaltiel, I.A., Datta, S., Lecomte, L., Hassler, M., Kschonsak, M., Bravo, S., Stober, C., Ormanns, J., Eustermann, S., and Haering, C.H. (2022). A hold-and-feed mechanism drives directional DNA loop extrusion by condensin. Science *376*, 1087–1094. https://doi.org/10.1126/science.abm4012.
64. Diebold, M.L., Fribourg, S., Koch, M., Metzger, T., and Romier, C. (2011). Deciphering correct strategies for multiprotein complex assembly by co-expression: application to complexes as large as the histone octamer. J. Struct. Biol. *175*, 178–188. https://doi.org/10.1016/j.jsb.2011.02.001.
65. Schindelin, J., Arganda-Carreras, I., Frise, E., Kaynig, V., Longair, M., Pietzsch, T., Preibisch, S., Rueden, C., Saalfeld, S., Schmid, B., et al. (2012). Fiji: an open-source platform for biological-image analysis. Nat. Methods *9*, 676–682. https://doi.org/10.1038/nmeth.2019.
66. Kabsch, W. (2010). Xds. Acta Crystallogr. D Biol. Crystallogr. *66*, 125–132. https://doi.org/10.1107/S0907444909047337.
67. Collaborative Computational Project Number 4 (1994). The CCP4 suite: programs for protein crystallography. Acta Crystallogr. D Biol. Crystallogr. *50*, 760–763. https://doi.org/10.1107/S0907444994003112.
68. McCoy, A.J., Grosse-Kunstleve, R.W., Adams, P.D., Winn, M.D., Storoni, L.C., and Read, R.J. (2007). Phaser crystallographic software. J. Appl. Crystallogr. *40*, 658–674. https://doi.org/10.1107/S0021889807021206.
69. Emsley, P., Lohkamp, B., Scott, W.G., and Cowtan, K. (2010). Features and development of Coot. Acta Crystallogr. D Biol. Crystallogr. *66*, 486–501. https://doi.org/10.1107/S0907444910007493.
70. Adams, P.D., Afonine, P.V., Bunkóczi, G., Chen, V.B., Davis, I.W., Echols, N., Headd, J.J., Hung, L.W., Kapral, G.J., Grosse-Kunstleve, R.W., et al. (2010). PHENIX: A comprehensive Python-based system for macromolecular structure solution. Acta Crystallogr. D Biol. Crystallogr. *66*, 213–221. https://doi.org/10.1107/S0907444909052925.
71. Williams, C.J., Headd, J.J., Moriarty, N.W., Prisant, M.G., Videau, L.L., Deis, L.N., Verma, V., Keedy, D.A., Hintze, B.J., Chen, V.B., et al. (2018). MolProbity: More and better reference data for improved all-atom structure validation. Protein Sci. *27*, 293–315. https://doi.org/10.1002/pro.3330.
72. Laue, T.M., Shah, B.D., Ridgeway, T.M., and Pelletier, S.L. (1992). Computer-aided Interpretation of Sedimentation Data for Proteins. Analytical ultracentrifugation in biochemistry and polymer science, 90–125.
73. Schuck, P. (2000). Size-distribution analysis of macromolecules by sedimentation velocity ultracentrifugation and lamm equation modeling. Biophys. J. *78*, 1606–1619. https://doi.org/10.1016/S0006-3495(00)76713-0.
74. Brautigam, C.A. (2015). Calculations and Publication-Quality Illustrations for Analytical Ultracentrifugation Data. Methods Enzymol. *562*, 109–133. https://doi.org/10.1016/bs.mie.2015.05.001.
75. Mastronarde, D.N. (2005). Automated electron microscope tomography using robust prediction of specimen movements. J. Struct. Biol. *152*, 36–51. https://doi.org/10.1016/j.jsb.2005.07.007.
76. Scheres, S.H.W. (2012). RELION: implementation of a Bayesian approach to cryo-EM structure determination. J. Struct. Biol. *180*, 519–530. https://doi.org/10.1016/j.jsb.2012.09.006.

77. Pettersen, E.F., Goddard, T.D., Huang, C.C., Couch, G.S., Greenblatt, D.M., Meng, E.C., and Ferrin, T.E. (2004). UCSF Chimera–a visualization system for exploratory research and analysis. J. Comput. Chem. *25*, 1605–1612. https://doi.org/10.1002/jcc.20084.

78. Meyerson, J.R., Rao, P., Kumar, J., Chittori, S., Banerjee, S., Pierson, J., Mayer, M.L., and Subramaniam, S. (2014). Self-assembled monolayers improve protein distribution on holey carbon cryo-EM supports. Sci. Rep. *4*, 7084. https://doi.org/10.1038/srep07084.

79. Westerfield, M. (2007). The Zebrafish Book 5th Edition - A Guide for the Laboratory Use of Zebrafish (*Danio rerio*) (University of Oregon Press).

80. Fribourg, S., Romier, C., Werten, S., Gangloff, Y.G., Poterszman, A., and Moras, D. (2001). Dissecting the interaction network of multiprotein complexes by pairwise coexpression of subunits in E. coli. J. Mol. Biol. *306*, 363–373. https://doi.org/10.1006/jmbi.2000.4376.

81. Romier, C., Ben Jelloul, M., Albeck, S., Buchwald, G., Busso, D., Celie, P.H.N., Christodoulou, E., De Marco, V., van Gerwen, S., Knipscheer, P., et al. (2006). Co-expression of protein complexes in prokaryotic and eukaryotic hosts: experimental procedures, database tracking and case studies. Acta Crystallogr. D Biol. Crystallogr. *62*, 1232–1242. https://doi.org/10.1107/S0907444906031003.

82. Vincentelli, R., and Romier, C. (2016). Complex Reconstitution and Characterization by Combining Co-expression Techniques in Escherichia coli with High-Throughput. Adv. Exp. Med. Biol. *896*, 43–58. https://doi.org/10.1007/978-3-319-27216-0_4.

STAR★METHODS

KEY RESOURCES TABLE

REAGENT or RESOURCE	SOURCE	IDENTIFIER
Bacterial and virus strains		
Escherichia coli BL21(DE3)	Invitrogen	Cat# C600003
Chemicals, peptides, and recombinant proteins		
LB Broth medium	Sigma	Cat# L3022-1KG
Isopropyl-1-thio-β-D-galactopyranoside (IPTG)	Sigma	Cat# I6758-1G
NaCl	Carlo Erba Reagents	Cat# 479687
Trizma Base	Sigma	Cat# T1503-1KG
Protease 3C	In-house	N/A
Magnesium chlorure hexahydrate	VWR international	Cat# 436994U
DL-Dithiothreitol (DTT)	Euromedex	Cat# EU0006
Tris(2-carboxyethyl)phosphine (TCEP)	Sigma	Cat# C4706-10G
Adenosine 5′-triphosphate (ATP)	Sigma	Cat# A26209-5G
Adenosine-5′-diphosphate (ADP)	Sigma	Cat# A2754-500MG
Adenosine 5'-(gamma-thiotriphosphate) (ATPγS)	Tocris Bioscience	Cat# 4080
Adenylyl-imidodiphosphate (AMP-PNP)	Euromedex	Cat# NU-407-50
2-Mercaptoethanol	Sigma	Cat# M3148-250ML
PACT crystallization screen	Molecular dimensions	Cat# MD1-29
JCSG+ crystallization screen	Molecular dimensions	Cat# MD1-37
Classics crystallization screen	Molecular dimensions	Cat# 130701
Wizard I and II crystallization screen	Molecular dimensions	Cat# MD15-W12-T
BCS crystallization screen	Molecular dimensions	Cat# MD1-104
LFS crystallization screen	Molecular dimensions	Cat# MD1-121
Glycerol	Sigma	Cat# G9012-100ML
PEG200	Sigma	Cat# P3015-250G
Dimethyl sulfoxyde (DMSO)	Sigma	Cat# D2650
Bismaleimidoethane (BMOE)	ThermoFisher	Cat# 9155
PBS	In-house	N/A
Tween 20	Sigma	Cat# P2287-500ML
Paraformaldehyde	Euromedex	Cat# EM-15710-S
Proteinase K	Thermo-Fisher	Cat# EO0491
Acridine orange	Sigma	Cat# A9231-10ML
Tricaine	PharmaQ	Cat# Tricaine PharmaQ 1000 MG/G
Critical commercial assays		
EnzChek Phosphate Assay kit	Fisher scientific	Cat# E6646
SP6 mMessage Machine kit	Fisher scientific	Cat# 32680
ApopTag® Fluorescein *In Situ* Apoptosis Detection kit	Millipore	Cat# S7110
Deposited data		
Crystallographic and cryo-EM structures	Protein DataBank (PDB)	PDB: 8ro6, 8ro7, 8ro8, 8ro9, 8roa, 8rob, 8roc, 8rod, 8roe, 8rof, 8rog, 8roh, 8roi, 8roj, 8rok, 8rol, 8p0a, 8pq5
Experimental models: Organisms/strains		
Zebrafish AB	Zebrafish International Resource Center (ZIRC)	Cat#ZL-1

(*Continued on next page*)

Continued

REAGENT or RESOURCE	SOURCE	IDENTIFIER
Zebrafish rad21a$^{hi2529Tg/+}$	Zebrafish International Resource Center (ZIRC)	Cat# ZDB-ALT-041006-8
Recombinant DNA		
pET-MCN vectors	In-house	Diebold et al.[64]
pCS2	In-house	N/A
Software and algorithms		
AFFINImeter	Affinimeter	N/A
FIJI	N/A	Schindelin et al.[65]
XDS	N/A	Kabsch et al.[66]
CCP4 suite	N/A	Collaborative Computational Project Number 4[67]
PHASERMR	N/A	McCoy et al.[68]
COOT	N/A	Emsley et al.[69]
PHENIX	N/A	Adams et al.[70]
MOLPROBITY	N/A	Williams et al.[71]
SEDNTERP	N/A	Laue et al.[72]
SEDFIT	N/A	Schuck et al.[73]
GUSSI	N/A	Brautigam et al.[74]
SERIALEM	N/A	Mastronarde et al.[75]
CRYOSPARC	Structura Biotechnology	N/A
RELION	N/A	Scheres et al.[76]
UCSF CHIMERA 1.15	N/A	Pettersen et al.[77]
GRAPHPAD PRISM v8.0.2.263	GraphPad Software	N/A
R v4.1.0	The R project for statistical computing	https://www.r-project.org/
PYMOL	Schrödinger	https://pymol.org/
Other		
Talon Superflow Metal Affinity Resin	Merck	Cat# GE28-9574-99
Hitrap Heparine HP	Dominique Dutscher	Cat# 17-0406-01
Superdex 200 Increase 10/300 GL	Dominique Dutscher	Cat# 28-9909-44
Hiload 16/60 Superdex 200 pg	Dominique Dutscher	Cat# 17-1069-01
Amicon ultra-0,5 Ultracel-30 membrane 30 kDa	Dominique Dutscher	Cat# 051852
Swissci 96-Well MRC Maxi Optimization Plates	Molecular Dimensions	Cat# MD11-00-10
Cryo-EM grids	N/A	Meyerson et al.[78]

EXPERIMENTAL MODEL AND STUDY PARTICIPANT DETAILS

The *Escherichia coli* BL21(DE3) bacterial strain used in this study is a commercially available *E. coli* strain that is required for the use of our pET-MCN vector series and of pET vectors in general. This strain was used and maintained using standard conditions for our study.

Zebrafish (*Danio rerio*) were raised and maintained as previously described.[79] Adult zebrafish were raised in 15 L tanks containing a maximum of 24 individuals, and under a 14 h–10 h light-dark cycle. The water had a temperature of 28.5°C and a conductivity of 200 μS and was continuously renewed. The fish were fed three times a day, with dry food and *Artemia salina* larvae. Embryos were raised in E3 medium, at 28.5°C, under constant darkness. AB wildtype and mutant *rad21a*$^{hi2529Tg/+}$ fish lines reproduce normally and *rad21a* homozygote mutants were recovered in expected Mendelian ratio. Homozygous *rad21a*$^{hi2529Tg/hi2529Tg}$ were not viable after 4 dpf. Developmental stages of zebrafish embryos and larvae are indicated in the text and figures. For zebrafish embryos and larvae, both males and females were used since the sex can only be determined at 2 months of age. All animal experiments were carried out according to the guidelines of the Ethics Committee of IGBMC and ethical approval was obtained from the French Ministry of Higher Education and Research under the number APAFIS#15025–2018041616344504.

METHOD DETAILS

Cloning

The SMC1A and SMC3 ATPase head domain (HD) constructs were generated by PCR using the full length human *smc1a* and *smc3* genes as templates. Specifically, short (SMC1ACCsh), up to the joint element (SMC1ACC and SMC3CC), and including the joint element (SMC1AJ and SMC3J) constructs were made (Figures 1A, S1 and S2). The sequences coding for the hinges and for the distal coiled-coils were replaced by sequences coding for a short protein linker (either ESSKHPASLVPRGS or GSGSLVPRGSGS), as previously reported.[6,8] The RAD21N and RAD21C constructs were generated by PCR using the full length human *rad21* gene as template. Point mutations were introduced into the constructions using rolling circle or nested PCR strategies. The constructs were cloned by Gibson assembly into bacterial pET-MCN co-expression vectors[64,80–82] to code either for native SMC1A-HD (SMC1ACCsh, SMC1ACC, SMC1AJ constructs) and SMC3-HD (SMC3CC and SMC3J constructs) or for RAD21 constructs (RAD21N and RAD21C) followed by a 3C protease cleavage site and a 10xhistidine fusion tag. Mini-expression tests showed that none of the constructs were soluble on their own. Co-expressions of the SMC1A-HD and RAD21C constructs and of the SMC3-HD and RAD21N constructs led however to soluble complexes, with the exception of the SMC1AJ/RAD21C complex that was poorly soluble.

Protein complexes production and purification

The same large-scale overproduction and purification methods have been used for all protein complexes, unless stated. The SMC1A- or SMC3-HDs-coding plasmids were respectively co-transformed with the RAD21C- or RAD21N-coding plasmids into chemically competent *Escherichia coli* BL21(DE3) cells. Co-transformed cells were selected using the appropriate antibiotics. Colonies were used to inoculate large cultures of 2x LB medium that were grown for 6 h at 37°C. Protein expression was induced at 25°C by the addition of a final concentration of 0.7 mM Isopropyl β-D-1-thiogalactopyranoside (IPTG), and cells were further grown overnight at 25°C. Culture media were discarded after centrifugation and the bacterial pellets from 3 L of culture were resuspended with 30 mL lysis buffer containing either 200 mM or 500 mM NaCl and 10 mM Tris-HCl pH 8.0. Pellets were stored at −20°C until further use.

After sonication, lysate clarification was performed by centrifugation (1 h at 17,000 rpm). The recombinant SMC1A-HD/RAD21C and SMC3-HD/RAD21N protein complexes were then purified by affinity chromatography using the 10xHis purification tag on RAD21 by incubating the cleared lysates with TALON Metal Affinity Resin. The purification tag was then removed on the affinity beads by overnight 3C protease digestion at 4°C. Removal of nucleic acid contaminants was performed using 1 mL or 5 mL HiTrap Heparin column and eluted using a NaCl gradient from 50 mM to 1 M. Peak fractions containing the protein complexes were pooled and further purified by size exclusion chromatography using a Hiload 16/60 Superdex 200 pg column equilibrated with a buffer containing 200 mM NaCl, 10 mM Tris-HCl pH 8.0, 2 mM $MgCl_2$ and either 1 mM TCEP (samples for crystallization and ITC assays) or 2 mM DTT (samples for ATPase assays). The main peak fractions with the protein complexes were pooled, concentrated with AMICON Ultra concentrator filters, and either used immediately or frozen in liquid nitrogen and stored at −80°C for later use.

ATPase assays

The ATPase activity of wildtype and mutant SMC1A-HD/RAD21C and SMC3-HD/RAD21N complex was assayed using the EnzChek Phosphate Assay Kit. For these assays, each protein sample (final concentration of 10 μM) was incubated with 1 mM ATP. After addition of ATP, the ATP hydrolysis activity was immediately assessed at 30°C, by measuring the absorbance at 360 nm every 42 s for 2 h, using a spectrophotometer plate reader (TECAN). The ATPase activities, expressed in Pi molecules released per dimer and per minute shown in the figures were calculated in the linear range of the curves. These experiments have been performed in technical and biological triplicates.

Isothermal titration calorimetry measurements

For ITC measurements, ATP, ATPγS or ADP were dissolved at a final concentration of 4 mM into the protein gel filtration buffer (200 mM NaCl, 10 mM Tris-HCl pH 8.0, 2 mM $MgCl_2$ and 1 mM TCEP). Each nucleotide was injected into 189 to 330 μM of either the wildtype or the EQ-mutant SMC1ACC/RAD21C or SMC3CC/RAD21N complexes, respectively. ITC measurements were performed at 5°C using a PEAQ-ITC microcalorimeter (Malvern Panalytical). ITC data were then corrected for the dilution heat generated by the injection of the buffer into the protein sample and of the nucleotide sample into the buffer.

ITC data were then fitted using the AFFINImeter analysis software. In most measurements, a single binding event was observed and processing was performed for a single binding event, which gave a good fitting of the experimental data. In the case of the SMC3CC/RAD21N complex two events were observed and the processing was made with a two binding events model. Since ADP binding to this complex led to a single event, we reasoned that the second binding event could be due to a homodimerization at high concentration of the SMC3CC/RAD21N complex in the presence of ATP and ATPγS. We therefore processed the ITC data for SMC3 with a model including two consecutive binding events: an initial ATP-binding event followed by a homodimerization event. This model gave a good fitting of the experimental data and yielded one Kd in the μM range and another in the low nM range for

the two events. Since the measured Kd of ADP for SMC3CC/RAD21N was in the μM range, we assumed that the Kd of ATP and ATPγS for the same complex also corresponded to the higher measured Kd. All measured thermodynamic parameters are given in Table S1.

Plots were made for each measurement to compare the entropic (e.g., change in the degree of disorder of the system) and enthalpic (e.g., relative strengths of the attractive and repulsive forces between the interacting molecules such as hydrogen bonds, van der Waals forces, Coulomb forces) contributions for each HD/nucleotide complex.

Crystallizations

Initial crystallization assays were carried out with commercial crystallization screens in swissci 96-Well 3-Drop MRC crystallization plates. Crystals were grown using the sitting-drop vapor-diffusion method at 4, 20°C and 27°C. Briefly, 200 nL of 4–15 mg/mL protein sample were mixed with 200 nL of reservoir solution. Several conditions from the commercial crystallization screens PACT, JCSG+, Classics, WIZARD I and II, BCS and LFS yielded protein crystals within a few hours up to several weeks. Some of the crystals, especially those from the SMC3-HD/RAD21N complex, required extensive optimization to improve their stability and diffraction limit. Selected crystals were cryo-protected with 20% (v/v) glycerol or 20% (v/v) PEG 200, then flash-cooled and stored into liquid nitrogen until data collection. Crystallization conditions are provided in Tables S2, S3 and S4.

Crystallographic structure determination, model building and refinement

X-ray diffraction data were collected at the SOLEIL and SLS synchrotrons. High resolution diffraction data (ranging from 1.4 to 3.1 Å) were obtained and processed by indexation, integration, and scaling within the XDS program. Data were merged using AIMLESS from the CCP4 software suite. The various SMC1A-HD/RAD21C and SMC3-HD/RAD21N structures were solved by molecular replacement using PHASERMR using respectively the yeast Smc1-HD/Scc1C (PDB: 1w1w) and Smc3-HD/Scc1N (PDB: 4ux3) structures as models. The initial models were subsequently iteratively built manually within COOT and refined using PHENIX. All refined models were verified with MOLPROBITY and showed good refinement statistics (Tables S2; S3; and S4).

Reconstitution of the ATP-engaged ATPase module by size exclusion chromatography

For the characterization of the stably engaged ATPase module by size exclusion chromatography, the WT or EQ independently purified SMC1ACC/RAD21C and SMC3CC/RAD21N complexes were supplemented or not with 0.5/1 mM of the different nucleotides (ADP, ATP, ATPγS, AMP-PNP), diluted to a concentration of 50 μM, and loaded onto a Superdex S200 10/300 column equilibrated with a buffer containing 200 mM NaCl, 10 mM Tris-HCl pH 8.0, 5 mM $MgCl_2$ and 1 mM TCEP, either without nucleotide or supplemented with 0.5/1 mM of the chosen nucleotide. The experiments with the WT and EQ, LV and DE mutants were performed initially using the same conditions but incorporating the SMC3J/RAD21N complex instead of the SMC3CC/RAD21N complex.

Reconstitution of the ATP-engaged ATPase module by analytical ultracentrifugation (AUC) experiments

Analytical ultracentrifugation sedimentation velocity experiments were performed with a ProteomeLab XL (Beckman Coulter) at 4°C and 42,000 rpm with absorbance detection at 280 nm. Independently purified SMC1ACC-EQ/RAD21C and SMC3CC-EQ/RAD21N complexes, stored in a buffer composed of 200 mM NaCl, 10 mM Tris-HCl pH 8.0, 5 mM $MgCl_2$ and 1 mM TCEP, were diluted to a final concentration of 1 mg/mL for experiments with the homodimers or mixed with a 1:0.9 ratio to a final concentration of 1 mg/mL for the heterodimers. ADP, ATP and low-hydrolysable ATP analogs (ATPγS, AMP-PNP) were added to the diluted samples at a concentration of 0.5/1 mM prior to measurements. The A280 nm scans data were acquired at 9 min intervals for 24h. The SEDNTERP software was used to estimate the partial specific volume of the protein (υ), the density (ρ), and the viscosity (η) of the samples. Data were analyzed in the SEDFIT software using the continuous c(s) distribution analysis. AUC graphs were rendered in the GUSSI software.

Cryo-electron microscopy sample preparation and data acquisition

For the preparation of the cryo-electron microscopy (cryo-EM) samples, the independently purified SMC1ACC-EQ/RAD21C and SMC3CC-EQ/RAD21N samples were mixed with a 1:0.9 ratio and loaded onto a Hiload 16/60 Superdex 200 pg column (GE Healthcare) equilibrated with the purification buffer (200 mM NaCl, 10 mM Tris-HCl pH 8.0, 5 mM $MgCl_2$ and 1 mM TCEP) supplemented with 1 mM ATP. The engaged complex obtained from the most concentrated chromatographic fraction was diluted to 0.3 mg/mL. A 3 μL aliquot of the sample was applied onto C-flat, Gold or in-house PEGylated gold 1.2/1.3 grids. The grid was blotted for 4s (blot force 5) and flash-frozen in liquid ethane using Vitrobot Mark IV (FEI) at 4°C and 100% humidity. Micrographs were acquired on a Glacios Cryo-TEM operated at 200kV on a K2 Summit camera in counting mode. Automated data acquisition was carried out using the SERIALEM software at a 45,000 magnification in a nanoprobe TEM mode, which yielded a pixel size of 0.901 Å. The defocus range was set from −0.8 to −2.0 or −3.0. 40 movies frames were recorded at a dose rate of 7.4 electrons per $Å^2$ per second to total doses of 43.61 up to 63.85 e/$Å^2$. A total of 11,313 micrographs were collected. Detailed collection data are provided in Table S5.

Cryo-electron microscopy data processing, model building and refinement

For all micrographs, motion-correction, dose-weighting and CTF estimation was performed in CRYOSPARC. Particles were picked in CRYOSPARC using first a blob picker job, followed by 2D classification. Templates were selected for template-based picking in Cryosparc, yielding a dataset of 7,098,916 particles. Subsequently, particles were extracted with a box size of 256 px and binned to

128 px. Two rounds of 2D classification were performed to clean up the dataset, and 1,037,793 particles were kept and used to generate 5 ab-initio maps. Three of these maps resembled to the engaged head model while the others two showed no particular features. Two rounds of heterogeneous refinement (with a box size of 64 px) were performed on the 5 maps to further clean up the dataset by keeping the particles belonging to the three recognizable classes generated by ab initio reconstruction. The remaining 652,840 particles were reextracted with a box size of 256 px and further cleaned up by two additional rounds of heterogeneous refinement. Eventually, the 174,054 and 144,776 particles corresponding respectively to the two best models were used in a non-uniformed refinement job. However, the map of the second model showed a significant level of noise due possibly to over-refinement. The corresponding particles and metadata were therefore exported from CRYOSPARC to RELION using the pyem conversion script. These were then imported in RELION3 and a new 3D refinement was performed followed by postprocessing. This resulting map had clearly improved details and no sign of over-refinement. The two cryo-EM maps issued from these different refinement steps have resolutions of 3.6 Å (first model) and 4.4 Å (second model).

Model building was performed using our crystal structures of the SMC1ACC/RAD21C, SMC1ACCsh/RAD21C and SMC3CC/RAD21N for docking into the 3.6 Å resolution cryo-EM map using UCSF CHIMERA. After manual adjustments, real-space refinement of the model was performed in PHENIX with secondary structure restraints, global minimization, morphing, and simulated annealing. The model was then further improved by several cycles of manual building/adjustment in COOT and real space refinement in PHENIX. Model validation was performed within COOT and with MOLPROBITY. This model was then used for docking into the cryo-EM map at 4.4 Å resolution and this second model was modified and refined using the same procedures as the first one, its lower resolution limiting modeling but enabling positioning of the secondary structure elements.

Of note, although particles corresponding to the engaged complex were observed in all collected datasets, those corresponding to the open-engaged complex were found mostly in datasets recorded with copper and gold grids, but much less with PEGylated-gold grids. This suggests that the loss of RAD21N was due to cryo-EM sample preparation, in agreement with the fact that this domain is not lost during purification of the engaged complex in the presence of ATP.

Cross-linking experiments

For crosslinking experiments, all endogenous cysteines of the SMC1ACC, SMC3CC, RAD21N and RAD21C constructs were mutated into serines to avoid initially observed unspecific crosslinking. The specific cysteines were then introduced in the SMC3CC (D92C and D120C) and RAD21N (K25C or K26C) constructs. Both SMC1ACC and SMC3CC ATP hydrolysis competent (E1157 and E1144) and impaired (E1157Q and E1144Q) complexes were used to investigate the effect of stable engagement. All complexes used were purified following the standard protocol described above. The SMC3CC/RAD21N complexes were mixed to a final concentration of 6 μM alone or in the presence of SMC1ACC/RAD21C (7 μM), ATP (20 μM), DNA (10 μM) and $MgCl_2$ (40 μM). Reactions were incubated for 5 min on ice or at room temperature before addition of 0.5 mM BMOE or DMSO. The reaction was quenched by addition of Laemmli buffer containing β-mercaptoethanol after 2, 5 and 10 min, and was further heated at 70°C for 5 min. The samples were loaded on acrylamide gel and band intensity was measured using FIJI. All experiments were performed in triplicates.

Zebrafish mutant line, *in vivo* complementation experiments and whole-mount immunostaining

Zebrafish (*Danio rerio*) were raised and maintained as described.[79] The mutant line *rad21a*$^{hi2529Tg/+}$ (AB genetic background) was obtained from the Zebrafish International Resource Center. The zebrafish line reproduces normally. The *rad21a* heterozygote mutant exhibits no phenotype. The *rad21a* homozygote mutants died at 4 days post-fertilization (dpf) from severe pericardial edema. For this study, viable heterozygous mutant adults were crossed and obtained larvae were individually scored and genotyped following the procedure previously described.[58] All the experiments were at least duplicated, all phenotypes were scored blind to the genotypes, and all statistical analyses were performed using GRAPHPAD PRISM and R.

For wild-type (WT) and mutant rescue experiments, *Danio rerio* WT and truncated *rad21a* constructs were cloned into the pCS2 vector, sequenced and transcribed using the SP6 mMessage Machine kit. 200 pg RNA (WT and/or mutants) were injected into mutant or WT zebrafish embryos at the 1- to 2-cell stage. Eye diameter, body curvature and pericardial edema were scored on injected larvae at 3 dpf fixed in 4% paraformaldehyde (PFA) and washed in PBS-Tween 0.1%. Body curvature and eye diameter were measured using FIJI and statistical differences were assessed using ANOVA followed by Tukey's test for post-hoc analysis. For edema scoring, embryos at 3 dpf were classified into three groups: none, mild, and severe based on the size of the edema compared with an age-matched control group from the same clutch and a Fisher's exact test was performed to determine significance.

For whole-mount TUNEL assay, apoptotic cell death in 1-day old zebrafish whole-mounts was detected according to a modification of the ApopTag Fluorescein *In Situ* Apoptosis Detection Kit protocol. Dechorionated embryos were fixed in 4% PFA at 4°C overnight and stored in 100% methanol at −20°C. After rehydration in PBS, embryos were digested with proteinase K (10 μg/ml) in PBS for 5 min at room temperature and washed 3 times in sterile water for 3 min each. Embryos were post-fixed with 4% PFA for 20 min at room temperature followed by a 10-min incubation in prechilled ethanol:acetic acid (2:1) at −20°C. Embryos were washed in PBS-Tween 0.1% for 5 min, 3 times at room temperature. Incubation in equilibration buffer and further steps were followed according to the manufacturer instructions. z stack image acquisition was performed using a MacroFluo ORCA Flash macroscope (Leica). TUNEL

staining was quantified by counting positive cells/dots in zebrafish head (forebrain, midbrain, eyes). Counting was performed using FIJI by combining automatic counting (ITCN plugin) with manual counting. Statistical differences were assessed with a t test with Welch's correction when necessary.

For acridine orange staining, one-day old embryos were dechorionated and incubated at 28°C for 30 min in E3 embryo medium supplemented with 2 μg/mL acridine orange. After extensive washing, embryos were anesthetized with tricaine and z stack imaging was performed with GFP green light excitation. Cell counting was performed with Fiji using the ITCN plugin. Statistical differences were assessed with a t test with Welch's correction when necessary.

Structural data

The structures described in this manuscript have been deposited under the following PDB codes: 8ro6, 8ro7, 8ro8, 8ro9, 8roa, 8rob, 8roc, 8rod, 8roe, 8rof, 8rog, 8roh, 8roi, 8roj, 8rok, 8rol, 8p0a, 8pq5.

Generation of the graphical supports

The figures have been generated with PYMOL, COOT, CHIMERA and GRAPHPAD PRISM. The videos have been generated with CHIMERA.

QUANTIFICATION AND STATISTICAL ANALYSIS

We used GRAPHPAD PRISM to visualize data. Statistical analyses were performed using either GRAPHPAD PRISM or R. All experiments from this study were performed at least on two biological replicates with at least 15 larvae per clutch. Adult zebrafish were raised from three independent clutches. When two groups were compared, normality of the distribution was assessed by performing a Shapiro-Wilk test. If the distribution was not normal, a Tukey test was conducted between pairs of conditions. If the distribution was normal, an F-test was conducted between pairs of conditions to assess whether the variances could be considered equal. If the variances were not statistically different, a Student's t-test was conducted between pairs of conditions. If the variances were statistically different, a Welch's t test was conducted between pairs of conditions. On dot plots, unless otherwise specified, the individual measurements are plotted, and the mean and standard deviation are represented. For qualitative data (e.g., classes based on the presence of cardiac edema), a Fisher's exact test was conducted between pairs of conditions to assess whether the distribution of samples in the different categories was significantly different. Two groups were considered statistically different if p-value <0.05. No data were excluded from analyses, unless otherwise specified in the results. Further quantification methodologies, details of specific statistical tests and statistical software used are included under the relevant subsections of the Methods details section and in figures and figure legends.